UCRL 384 Rev.
cy. 2

UNIVERSITY OF CALIFORNIA

Radiation Laboratory

TWO-WEEK LOAN COPY

This is a Library Circulating Copy which may be borrowed for two weeks. For a personal retention copy, call Tech. Info. Division, Ext. 5545

BERKELEY, CALIFORNIA

DISCLAIMER

This document was prepared as an account of work sponsored by the United States Government. While this document is believed to contain correct information, neither the United States Government nor any agency thereof, nor the Regents of the University of California, nor any of their employees, makes any warranty, express or implied, or assumes any legal responsibility for the accuracy, completeness, or usefulness of any information, apparatus, product, or process disclosed, or represents that its use would not infringe privately owned rights. Reference herein to any specific commercial product, process, or service by its trade name, trademark, manufacturer, or otherwise, does not necessarily constitute or imply its endorsement, recommendation, or favoring by the United States Government or any agency thereof, or the Regents of the University of California. The views and opinions of authors expressed herein do not necessarily state or reflect those of the United States Government or any agency thereof or the Regents of the University of California.

COPY 2
UCRL-384

Revised

Unclassified Distribution

UNIVERSITY OF CALIFORNIA

Radiation Laboratory

UNCLASSIFIED

Contract No. W-7405-eng-48

THE NEUTRON-PROTON INTERACTION

Richard S. Christian and Edward W. Hart

September 21, 1949

Berkeley, California

Unclassified Distribution

Standard Distribution	No. Copies
Argonne National Laboratory	8
Armed Forces Special Weapons Project	1
Atomic Energy Commission, Washington	2
Battelle Memorial Institute	1
Brookhaven National Laboratory	8
Bureau of Medicine and Surgery	1
Bureau of Ships	1
Carbide & Carbon Chemicals Corp. (K-25)	4
Carbide & Carbon Chemicals Corp. (Y-12)	4
Chicago Operations Office	1
Cleveland Area Office	1
Columbia University (Dunning)	1
Columbia University (Failla)	1
Dow Chemical Company	1
General Electric Company, Richland	6
Hanford Operations Office	1
Idaho Operations Office	1
Iowa State College	2
Kansas City	1
Kellex Corporation	2
Knolls Atomic Power Laboratory	4
Los Alamos	3
Mallinckrodt Chemical Works	1
Massachusetts Institute of Technology (Gaudin)	1
Massachusetts Institute of Technology (Kaufmann)	1
Mound Laboratory	3
National Advisory Committee for Aeronautics	2
National Bureau of Standards	2
Naval Radiological Defense Laboratory	2
NEPA Project	2
New Brunswick Laboratory	1
New York Operations Office	5
North American Aviation, Inc.	1
Oak Ridge National Laboratory	8
Patent Advisor, Washington	1
Rand Corporation	1
Sandia Base	1
Sylvania Electric Products, Inc.	1
Technical Information Branch, ORE	15
U. S. Public Health Service	1
UCLA Medical Research Laboratory (Warren)	1
University of California Radiation Laboratory	5
University of Rochester	2
University of Washington	1
Western Reserve University (Friedell)	2
Westinghouse	4
Total	119

Unclassified Distribution

The Neutron-Proton Interaction

Richard S. Christian and Edward W. Hart

Radiation Laboratory, Department of Physics
University of California, Berkeley, California

September 21, 1949

Introduction

The purpose of the present paper is to ascertain if it is possible to determine a phenomenological description of the neutron-proton interaction in terms of a potential. A further aim is to determine with what uniqueness this potential can be determined from the present experiments, particularly those at high energies. The program will be to assume a number of potential models so adjusted that they fit the low energy region and attempt to correlate the high energy scattering with the various features of each model.

It is well known that the experimental results in the low energy region can be described by an interaction potential; however, for sufficiently high energies relativistic corrections may be expected to be of major importance. Detailed scattering calculations, using a field theory, show that the use of relativistic momenta corresponds to calculating the kinematical aspects relativistically, but that the dynamical corrections depend on the specific theory employed. Scattering deduced from a field theory(1) has, in general, relativistic correction proportional to $(v/c)^2$; for example, at 90 Mev $(v/c)^2$ is 0.05 while approximately 10 percent corrections are found by application of the Møller method to the scalar and vector meson theories.(2) Thus a choice cannot be made between two models both of which agree within 10 percent with the experimental results at 90 Mev.

The experimental results of the low energy region (including some derived quantities) are summarized in Table 1. None of these experiments give information concerning the explicit radial dependence of the forces or of the forces in other than S-states, and, in fact even the ranges are determined only approximately. In the triplet state there is a further uncertainty in the relative central and tensor ranges. This latter uncertainty would be removed considerably if it were assumed that the magnetic moment gave a measure of the D-state admixture due to tensor forces. Unfortunately because of uncertain relativistic corrections[3] this forms an unreliable restriction. The depths of the various potentials, i.e., singlet and triplet central and triplet tensor, are, however, accurately determined for any specified combination of ranges.

The high energy experimental angular distributions are shown in graphical form in Fig. 1. The expansion (in Legendre polynomials, $P_n(\theta)$) for the 90 Mev distribution is

$$4\pi \cdot \sigma(\theta) = \sigma\left[1 - 0.14\, P_1(\theta) + 0.73\, P_2(\theta) + 0.08\, P_3(\theta) + 0.17\, P_4(\theta)\right] ,$$

with an estimated error of ± 0.1 for the coefficients of $P_1(\theta)$ through $P_4(\theta)$. The most noteworthy result is the near symmetry about 90°. We have therefore assumed that the 40 Mev angular distribution, which has been determined only in the range 70°-180°, is symmetrical about 90° with the consequent expansion

$$4\pi\sigma(\theta) = \sigma\,(1 + .26\, P_2(\theta) + .02\, P_4(\theta)\ ) ,$$

with an estimated error of ± 0.1 for the $P_2(\theta)$ and $P_4(\theta)$ coefficients. The experimental total cross sections are tabulated in Table 2. The low values for the total cross sections appear to be further corroboration of the lack of odd harmonics in scattering.

A unique analysis into phase shifts of the experimental angular distribution is impossible due to the presence of the mixture of singlet and triplet states

as well as the complication of the tensor force. Nevertheless, on the simplifying assumption of scattering with no spin dependence, the 90 Mev angular distribution may be analyzed to give the order of magnitude of the phase shifts. The results of this are: S-wave, $53^{\circ} \pm 5^{\circ}$; P-wave, $-1^{\circ} \pm 1^{\circ}$; D-wave, $5^{\circ} \pm 1^{\circ}$. Since the P and D phase shifts are so small, we may conclude that at 90 Mev the S scattering accounts for about 90 percent of the total scattering cross section. The high energy cross sections, therefore, determine the S scattering fairly unambiguously. The potentials usually considered show significant differences in S scattering above 30-40 Mev when adjusted to have the same low energy properties. The comparison then of the S-wave cross sections provides one method of determining the potential shape.

The angular distribution at a particular energy yields information primarily concerning the exchange character of the forces. For example, theories such as the "charged" or "neutral" which predict large scattering in odd states may be immediately discarded as unacceptable. The low values of the high energy cross sections also favor theories without large scattering in odd states.

Finally, comparison of angular distributions at two or more high energies enables one to distinguish shape features of the various potentials. This final comparison is a critical test of the potential shape since, while it is possible with any shape, by a proper choice of range, to fit the angular distribution at 90 Mev and the low energy data simultaneously, it will not in general, be possible to also fit the 40 Mev angular distribution.

Computational Methods

Various approximate methods were employed to avoid the many tedious numerical integrations required for a comprehensive investigation of the effect of the many parameters. These are principally concerned with the integration of

the radial equations to yield phase shifts or eigenvalues.

Most of the calculations were done by iteration of trial functions in the integral form of the equations. In order that this procedure might converge rapidly, it was necessary to have good initial trial functions, especially in the case of potentials with a deep hole at the origin. Suitable trial functions were provided by the WKB approximation (explicitly using 1/3 order Bessel functions as the asymptotic representations).[14] This approximation has been further extended to the case of coupled equations as follows.

Let the differential equations to be solved be:

$$u'' + A(x)u + B(x)w = 0$$

$$w'' + C(x)w + B(x)u = 0 \ .$$

The desired representation of the solution is then

$$u = \cos\eta \cdot (S/S')^{1/2} \, Z_{1/3}(S)$$

$$w = \sin\eta \cdot (S/S')^{1/2} \, Z_{1/3}(S) \ .$$

where

$$(S'_{\pm})^2 = \frac{1}{2}\left\{ A + C \pm \left[(A-C)^2 + 4B^2\right]^{1/2} \right\} \ ,$$

$$\tan\eta = (S'^2_{\pm} - A)/B \ .$$

The + and − signs correspond to two independent representations. The Z's are Bessels functions of order 1/3. The usual phase integral condition for the bound state is replaced by the similar condition,

$$\int_{x_1}^{x_2} S' dx = S_n \ ,$$

where x_1 and x_2 are the turning points and S_n is a root of

$$\frac{d}{dS}\,(S)^{1/2}\left[J_{1/3}(S) + J_{-1/3}(S)\right] = 0 \quad .$$

These representations have been found to yield close approximations to the wave functions at all energies, the S-wave phase shifts being in general in error by less than five degrees, and the wave functions exhibiting the correct general behavior. When applied to the bound state, the phase integral condition yields potential depths that are within 10 percent of the correct value.

The bound deuteron state was numerically iterated using the variation-iteration[15] method, using as a trial function the approximate WKB functions above. Three iterations yielded an eigenvalue and wave functions with an accuracy of about one percent. The accuracy was essentially limited by the numerical methods used (intervals corresponding to one to two tenths of the effective range were used).

For the $^3S_1 + {}^3D_1$ scattering state the appropriate WKB functions above furnished trial functions for the coupled integral system

$$u = A \sin kx + M/\hbar^2 \int_0^\infty G_0(kx, kx')\left[V_c(x')u(x) + 2^{3/2}\gamma\, V_t(x')w(x')\right] dx'$$

$$w = B\, g_2(kx) + M/\hbar^2 \int_0^\infty G_2(kx, kx')\left\{\left[V_c(x') - 2\gamma V_t(x')\right] w(x') + 2^{3/2}\gamma V_t(x')u(x')\right\} dx',$$

where A = 1, B=0 corresponds to the choice of the positive sign in $(S_{\pm}^{\dagger})^2$ and $A = \frac{M}{\hbar^2 k}\int_0^\infty \cos kx\left[V_c(x')u(x') + 2^{3/2}\gamma\, V_t(x')w(x')\right] dx'$, B=1 corresponds to the negative sign. Further

$$G_0(kx, kx') = (1/k)\sin kx_< \cos kx_>$$

$$G_2(kx, kx') = (1/k)^3\, g_2(kx)_<\, k^2\, g_{-2}(kx)_> \quad ,$$

where $x_<$ means the lesser of x and x'.

The potential has been written in the form

$$V(r, \sigma) = V_c(r) + \gamma\, S_{12}\, V_t(r) \quad .$$

The iteration of the integral equations above was carried out numerically with the normalization of the trial functions so chosen that the iterated functions matched the trial functions in the region where the kernel of the integral system is largest. Three iterations for the S-dominant mode (i.e., with $A = 1$, $B = 0$) and one for the D-dominant mode yielded phase shifts with an accuracy of about 2 percent.

The phase shift in the $^3D_2$ state was calculated using the variational procedure with the $^3D_2$ component of the plane wave as a trial function. The phase shift in the $^3D_3 + {}^3F_3$ state was computed using the same procedure as for the $^3S_1 + {}^3D_1$ state. One iteration yielded an accuracy of two percent.

The Born approximation was used to effect the inclusion of the angular momentum states for $\ell \geq 4$ in the scattering sum. The sum was, in general, done by actually summing the individual terms for $\ell \leq 3$, using calculated phase shifts, and adding the Born cross section from which these states had been suitably subtracted. The angular distributions so derived are accurate within 2-5 percent.

Central Forces

We shall consider in this section the results of scattering from a model which consists only of central forces since, as will be seen later, it is possible to make a state by state comparison of the scattering from a central force model and from one which includes tensor forces.

The details of low energy scattering will not be treated here, but, rather, the reader is referred to the review of Blatt and Jackson.[16] One result of their work is that in the expansion

$$k \cot {}^3\delta_S = -(1/{}^3a) + 1/2({}^3r)k^2 - {}^3Tk^4 + \ldots$$

the shape dependent coefficient, T, is sufficiently small that below 6 Mev

it can be neglected, and, in interpreting the experiments, the shape independent approximation may be used. The effective range in the triplet state is determined, therefore, by the approximate relation

$$(1/{}^3a) = (1/r_d) \left[1 - 1/2\ ({}^3r/r_d)\right]$$

Substituting the experimental values from Table 1, we obtain

$${}^3r = 1.53 \pm .20 \times 10^{-13}\ \text{cm.}$$

Fig. 2 is a plot of effective range versus intrinsic range for the triplet state of the various potentials. The singlet effective range is not well determined by the present experiments, as can be seen by reference to Figs. 3 and 4.

To simplify the analysis of the high energy data, it is convenient (and reasonable) to assume exact symmetry of scattering about 90 degrees. This means that the potential is assumed to be zero in odd parity states. The experimental results are actually compatible with a small repulsive potential in odd states, but this shall be considered as a small perturbation which will not essentially alter any of the following conclusions. The factor $\frac{1}{2}(1 + P_x)$ will, therefore, be included as a factor in the potential and will have as one consequence that the total cross section computed for any radial dependence will be the minimum possible over any other choice of exchange dependence. The main effect of any admissible odd wave phase shifts is the interference with the large S-wave phase shift, which is in evidence only in the angular distribution, and its actual effect on the total cross section is negligible.

In order to compare different potential shapes, the effective range has been taken as a common parameter. For example, we have plotted (Fig. 5) the S-wave phase shift at 90 Mev for the various potentials versus the effective range. This device insures similar low energy behavior for the same abscissa.

In Fig. 6 are plots at 90 Mev for the various potentials of the total cross section and of 4π times the differential cross section for scattering at 90° and 180° as functions of the effective range on the assumption of no odd parity interaction. For the plots of complete total cross section, i. e., the sum of triplet and singlet scattering, it is necessary to make some choice of a singlet range corresponding to a particular triplet range. The low energy region implies only loose restrictions on the singlet range; we may, therefore, choose the singlet range so that the singlet and triplet intrinsic ranges are equal. The results for the complete cross sections are also shown in Fig. 6. From these plots it is possible to make further limitations on the allowable triplet ranges by a comparison with the experimental values of $\sigma(180^{\circ})/\sigma(90^{\circ})$.

With the Yukawa or exponential potential a range adjusted for the 90 Mev ratio predicts a 40 Mev ratio within the experimental limits. However, with the square well potential, the range required at 40 Mev is considerably larger than that required at 90 Mev. This difference in behavior results primarily from the more rapid decrease in $\sigma(90^{\circ})$ with energy increase for the "cut-off" potential than for the "long-tailed" potentials. This, in turn, can be interpreted in terms of the destructive interference between the S and D waves at 90 degrees. In detail, the S-wave phase shift decreases more rapidly (as a function of energy) for the "cut-off" potentials (Fig. 7). Further the D-wave phase shift is nearly a linearly increasing function of energy for the "long-tailed" potentials, while the increase with energy is much more rapid for the "cut-off" potentials (Fig. 8).

For potentials which have a "deep hole" at the origin (e.g., the Yukawa and exponential) the "long-tail" is necessary to give a sufficiently long effective range. However, as the energy increases the contributions to the S-wave phase shift come from regions closer to the origin, and, consequently, at high energies the "deep hole" (and, therefore, "long-tailed") potentials yield larger

phase shifts than the "cut-off" potentials (e.g., the square well or gauss potentials). These remarks are further illustrated by reference to Figs. 5 and 7.

While it is impossible to define the limits of the singlet effective range with any accuracy, for $^3r < 1.7 \times 10^{-13}$ cm the best fits for the angular distribution are obtained with the singlet effective range between $2.5 - 3.0 \times 10^{-13}$ cm.

The complete angular distribution is shown in Figs. 9 and 10, for the Yukawa and exponential potentials with ranges chosen such that they are both good fits of the angular distribution at 90 Mev. From this the superiority of the Yukawa angular distribution at 40 Mev is apparent. The total cross sections, however, are in much better agreement with the exponential potential.

The only partial waves contributing appreciably to the cross sections are the S- and D-waves, consequently the angular distribution can be expanded in terms of Legendre polynomials P_o, P_2 and P_4. The coefficient of P_o is identical with the total cross section, that of P_2 arises primarily from the interference between the S- and D-states, and that of P_4 arises primarily from the combinations of the various D-states. These coefficients allow a rapid comparison of theory and experiment and are therefore tabulated in Table 3 for all models mentioned explicitly.

If we consider the Yukawa and exponential potentials of Figs. 9 and 10, we see that the only discrepancy with the experimental values of the coefficients occurs in the magnitude of the P_4 coefficient which is perhaps a factor of two to three too large. This is manifested in the angular distribution by a theoretical prediction that is somewhat too flat in the region about 90°.

Fig. 9 and Table 4 show the effect of adding a small repulsive potential in the odd parity states. This modification may be expressed by a potential factor, $(1 - a + aP_x)$. The best fit for this type of exchange interaction is $a = 0.55 \pm 0.05$.

The large odd state potentials in the singlet state required by the symmetrical theory produces far too much exchange scattering for any potentials with a tail and a range compatible with low energy scattering. For "cut-off" potentials such as the square well the observed ratio $\sigma(180^\circ)/\sigma(90^\circ)$ may be fitted at 90 Mev with a range of $1.7 - 1.8 \times 10^{-13}$ cm; however, at 40 Mev, a fit to $\sigma(180^\circ)/\sigma(90^\circ)$ would require a range longer than 2.0×10^{-13} cm. Furthermore, in these latter cases the shape of the predicted angular distribution is not similar to the experimental results for small angle scattering. The symmetrical theory can, therefore, be ruled out for central forces.

Tensor Forces

A. The bound state and low energy scattering

The existence of the deuteron quadrupole moment requires the inclusion of a tensor potential in the neutron-proton interaction. We consider first the case where the radial dependence is chosen the same for both the central and tensor potentials. The extreme cases of "long-tailed" and "cut-off" potentials are exemplified by the Yukawa and square well respectively. Calculation, of the quadrupole moment have been made for these potentials as a function of range and tensor depth with the central depth adjusted to give the correct binding energy. The results are presented graphically in Figs. 11, 12 and 13.

The calculations of Rarita and Schwinger[22] have shown that at least for the choice of a square potential, there is only slight modification of the low energy scattering properties upon the introduction of tensor forces. Such a behavior can be expected for more general potential shapes with ranges shorter than the deuteron radius since the S-wave component is determined primarily from the boundary conditions at the origin and asymptotically.[23]

We can put these arguments on a quantitative basis by the consideration of an "equivalent central potential," "V(r)." For the potential $V(r) = V_c(r) + \gamma S_{12} V_t(r)$, the "equivalent central potential" for the S-wave is

$$"V(r)" = V_c(r) + 2^{3/2} \gamma V_t(r) \cdot R(r) ,$$

where R(r) is the ratio of the D-wave to the S-wave, R(r) will be, in general, a slowly varying function of the energy (at least in the region where the potential is large). Its form may then be estimated from considerations of the bound state solutions. It is found then that R(r) is zero at the origin, increases to a maximum value (about 0.2 or 0.3) somewhere between the maximum of the S-wave radial function and the tensor force range, and decreases symptotically to a small value (somewhere under 0.1). Then if we consider the ratio of the equivalent potential "V(r)" to the central potential $V_c(r)$ (the latter adjusted to give binding by itself), we would find the ratio to be less than unity at the origin, greater than unity in the neighborhood of the range, and again less than unity asymptotically. Thus the equivalent potential will be shallower at the origin and asymptotically, and will be deeper in the neighborhood of the tensor range.

This can be further illustrated in terms of the WKB approximation. In this approximation, R(r) is independent of energy and decreases asymptotically to zero. The equivalent potential in this approximation is

$$"V" = V_c - \gamma V_t - \frac{3}{r^2} + \left[\left(\gamma V_t + \frac{3}{r^2}\right)^2 + 8 (\gamma V_t)^2 \right]^{1/2}$$

If the centrifugal potential is large compared to the tensor potential, this may be simplified to

$$"V" = V_c + \frac{4}{3} (\gamma r V_t)^2$$

which is clearly in agreement with the preceding remarks.

The analysis of the low energy scattering is again conveniently carried out in terms of the expansion of the phase shift in powers of the energy.[24] Since the shape independent approximation is valid for Yukawa ranges less than 1.4×10^{-13} cm and for all square well ranges considered, the effective range is essentially

determined from the triplet scattering length. (The explicit value of the shape dependent coefficient as well as the effective ranges are shown in Table 4 for a number of cases.) We have chosen, therefore, in order to relate the scattering characteristics of a potential with its ability to produce a quadrupole moment, to plot $1/\gamma$ versus the scattering length (Fig. 14) with the range indicated parametrically along the curves. From this plot we can conclude that with the accepted value of the scattering length, the proportion of tensor potential must be quite large, the actual amount being lower for the long-tailed potential.

The low energy constants for the case in which the tensor force range is increased relative to the central force range are given in Table 4 and Fig. 15. From the equivalent potential we see that the main effect is to increase the "long-tailed" character of the potential. This is evident by the decrease in the percentage D state and by the increase in the shape dependent coefficient.

B. High energy scattering

We will attempt in the next paragraphs to gain a qualitative understanding of the relation between central and tensor scattering. Then we will consider the results of various models, the calculations being carried out by the methods previously described.

As in the case of central forces we must adjust the ranges so that only the S- and D- partial waves contribute to the cross section. We would then expect that if the tensor force were a weak effect we could add the tensor scattering which would be present in Born approximation. Actually, as we have seen, the tensor force is far from weak and the approximation can only be expected to give the general trend. The characteristic peaking of the Born-approximation cross section around 45 and 135° (the exact angle depending upon the model, range and energy with a maximum occurring roughly where $2kR \sin \theta/2 \sim 1$) is, in fact, the type of correction needed to explain the discrepancy between the shapes of the

experimental curves and the central force curves shown in Figs. 9 and 10, i.e., such a correction could convert the U-shaped central force curves into the more V-shaped experimental curves.

For a somewhat more detailed comparison we will again use the WKB approximation to approximate the "equivalent central potentials," "V_L^J," for each of the states L and J, with the result

$$"V_0^1" = V_c - \gamma V_t - \frac{3}{r^2} + \left[\left(\frac{3}{r^2} + \gamma V_t\right)^2 + 8(\gamma V_t)^2\right]^{1/2}$$

$$\approx V_c + \frac{4}{3}(\gamma r V_t)^2$$

$$"V_2^1" = V_c - \gamma V_t - \frac{3}{r^2} - \left[\left(\frac{3}{r^2} + \gamma V_t\right)^2 + 8(\gamma V_t)^2\right]^{1/2}$$

$$\approx V_c - 2\gamma V_t + \frac{4}{3}(\gamma r V_t)^2 - \frac{6}{r^2}$$

$$"V_2^2" = V_c + 2\gamma V_t - \frac{6}{r^2}$$

$$"V_2^3" = V_c - \gamma V_t - \frac{13}{r^2} + \left[\left(\frac{7}{r^2} + \frac{3}{7}\gamma V_t\right)^2 + 3\left(\frac{12}{7} V_t\right)^2\right]^{1/2}$$

$$\approx V_c - \frac{4}{7}\gamma V_t + \frac{3}{14}\left(\frac{12}{7}\right)^2 (\gamma r V_t)^2 - \frac{3}{r^2}$$

In the approximation where we neglect the asymptotic amplitude of the coupled mode, as above, in the evaluation of the phase shifts there will be no difference between states of different magnetic quantum number, m_s, however the WKB approximation yields angular distributions which agree with the results of a more accurate calculation within 10 to 20 percent.

long-tailed potentials such as the exponential or the Yukawa potential.

The results of using the Yukawa and exponential radial dependences (cf. Figs. 16, 17 and 18) indicate that the addition of tensor forces causes only relatively small changes in the scattering. The best fits of the angular distribution require slightly longer ranges than for the purely tensor model. A detailed comparison, using the Legendre coefficients, shows that the $P_4(\theta)$ component is reduced in the tensor model. It is this decrease which allows considerably better fits of the angular distribution and is therefore evidence for the presence of tensor forces in scattering. The total cross section is increased, however, approximately 10 percent with the addition of tensor forces so that the agreement with the experimental value of the total cross section is poorer.

The same situation holds for the tensor model as for the central model regarding the intercomparison of the Yukawa and exponential potentials. That is, the Yukawa potential fits the angular distributions at both 40 and 90 Mev noticeably better, however the total cross section is 20 to 30 percent too high. The total cross section with the exponential potential is only 10-15 percent too high. Since the "long-tail," which is necessary to fit the angular distribution, forces the potentials considered here to also have a "deep hole" and consequently high cross section, it would seem that an essentially more complicated radial dependence would be necessary to fit the experimental results more closely. It is believed, though, that the present experimental data (as well as uncertain relativistic effects) do not exclude either the Yukawa or exponential potentials.

The exchange character found necessary for the central force model is also valid, in the main, for the tensor force model (cf. Table 3). As an example of spin dependent exchange dependence we have considered the case when the central force has a $\frac{1}{2}(1 + Px)$ exchange dependence and the tensor force exchange dependence was of the form $(1 + a - aPx)$. This does not produce as large asymmetries in the

angular distribution as when $(1 + a - aP_x)$ is taken as a factor of both the central and tensor potential. The restriction on the magnitude of a, now arises mainly from the increase in the total cross section. These limits are estimated to be $a = 0.6 \pm 0.1$.

The principal change in the high energy scattering with increase in tensor range, is according to the WKB arguments, similar to an increase in the "long-tailed" character of the potential. The high energy scattering results are shown in Fig. 19 for the cases listed in Table 4. There is an increase in scattering from the higher states which may be interpreted as the increase in the "long-tailed" character or alternatively as showing that the characteristic Born approximation tensor peaking is displaced to smaller angles.

We wish to note here that all of the models seriously considered (because of the smallness of the odd state potentials) predict nearly isotropic distribution at 14 Mev in agreement with the recent experiments of Barschall and Taschek[27] who find isotropy within their statistical accuracy of 6 percent.

Conclusions

1. Exchange character. If the potential has approximately the same radial dependence in all states (i.e., even and odd parity, singlet and triplet) and the range is chosen within acceptable limits, we may conclude that for a good fit

$$a = 0.55 \pm 0.05$$

or, alternatively, the depths of odd potentials, V_{odd}, must satisfy the relation

$$0 > ({}^1V_{odd}) + ({}^3V_{odd}) > - ({}^3V_{even})$$

2. Radial dependence. The $(1 + P_x)/2$ potentials, when compared for equal effective ranges differ by at most a factor of 2 in the total cross section or in the ratio $\sigma(180^\circ)/\sigma(90^\circ)$. However, these differences may be correlated with general shape features. Further the experiments are adequate to distinguish

among the potential shapes.

a. A long-tailed potential is necessary to explain the large scattering from the higher angular momentum states at 40 Mev without violently affecting the 90 Mev scattering. On this basis the square and gauss potentials are unacceptable while the exponential and Yukawa potentials are allowable.

b. The Yukawa potential, because of its singular nature, predicts high total cross sections (approximately 20 to 30 percent higher than the best experimental value) for any combination of ranges. The exponential potential for approximately the same angular dependence predicts cross sections 10 percent to 20 percent lower, however, the detailed fit of the angular distribution is poorer. Both are acceptable, however, with the present experimental uncertainties.

The best fit for these potentials is (assuming the same range for all the forces)

$$R = 0.75 \times 10^{-13} \text{ cm} \quad \text{(exponential)}$$

$$R = 1.35 \times 10^{-13} \text{ cm} \quad \text{(Yukawa)}$$

(For calculations, where the tensor force is unimportant a central force model with a Yukawa range of 1.18×10^{-13} cm can be used.)

c. The shape of the angular distribution about 90° is evidence of a tensor force in scattering. Here, with a $\frac{1}{2}(1 + P_x)$ dependence, a purely central force yields a flatter distribution than an interaction including tensor forces. The latter distribution agrees significantly better with experiment.

3. Singlet range. The total cross section measurements imply a singlet effective range greater than 2×10^{-13} cm. A long singlet range is further favored by the angular distribution. Low energy scattering yields only the requirement that the singlet range be less than 3×10^{-13} cm.

4. Triplet range. The low energy limits on the effective range are $1.53 \pm .20 \times 10^{-13}$ cm. The determination of the limits on the range from high energy scattering depend upon the explicit model used but for all models considered

it has been found to be within the above limits.

5. Tensor force range. The tensor range may be increased relative to the central range by as much as a factor of 2 without adversely affecting either the low or high energy results.

Acknowledgments

The authors wish to express their thanks to Professor Robert Serber for continued guidance in the general theory and in interpretation of the experiments. We also wish to thank Messrs. Richard Huddelstone and Donald Swanson for aid and suggestions with the calculations. This work was carried out under the auspices of the Atomic Energy Commission.

Information Division
9-26-49/hw

Table 1

Derived Quantities

Quantity	Notation	Magnitude	Source (with error)
singlet scattering length	1_a	$-23.70 \pm .10 \times 10^{-13}$ cm	ortho-para scattering[4] ($\pm$ 0.03 x 10^{-13} cm) crystal-scattering[5] ($\pm$ 0.05 x 10^{-13} cm) zero energy cross section[6] ($\pm$ 0.06 x 10^{-13} cm)
radius of deuteron	r_d	$4.332 \pm .025 \times 10^{-13}$ cm	binding energy[7]
triplet scattering length	3_a	$5.26 \pm .12 \times 10^{-13}$ cm	ortho-para scattering ($\pm$ .09 x 10^{-13} cm) crystal scattering ($\pm$ .15 x 10^{-13} cm) zero energy cross section ($\pm$ .03 x 10^{-13} cm)
triplet effective range (shape ind. approx.)	3_r	$1.53 \pm .20 \times 10^{-13}$ cm	from 3_a ($\pm$ .17 x 10^{-13} cm) from r_d ($\pm$ .03 x 10^{-13} cm)
singlet effective range	1_r	$< 3 \times 10^{-13}$ cm	scattering between 0 and 6 Mev
electric quadrupole moment	Q	$2.73 \pm .05 \times 10^{-27}$ cm^2	directly determined[8]
percent D-state	W_D	3.9 percent	magnetic dipole moment, neglecting relativistic effects

Table 2

High Energy Total Cross Sections

Mean Energy Mev	Total cross section with statistical error 10^{-24} cm	Detection method	Average $\sin^2\delta_s$	Ref.
41 ± 4	.174 ± .010	Proton recoils	.67 ± .11	(9)
40 ± 4	.202 ± .007	$C^{12}(n,2n)C^{11}$	.76 ± .11	(10)
83 ± 7	.083 ± .004	$C^{12}(n,2n)C^{11}$	.66 ± .08	(11)
90 ± 3	.079 ± .007	Proton recoils	.68 ± .08	(9)
95 ± 5	.073 ± .002	Bi fission	.66 ± .06	(12)

The error in the mean energy arises from uncertainties in detector efficiency, neutron beam distribution, and variation of cross section with energy.

The "average" $\sin^2\delta_s$ is determined by subtracting the contributions of the higher partial waves as derived from the angular distribution on the basis of no spin dependence in scattering.

Table 3

Model				90 Mev							40 Mev		
Exchange Dependence	Range (10^{-13} cm)	Radial Dependence	γ	σ (10^{-26} cm^2)	a_1	a_2	a_3	a_4	$\frac{\sigma(180)}{\sigma(90)}$	$\frac{\sigma(0)}{\sigma(90)}$	σ (10^{-26} cm^2)	a_2	$\frac{\sigma(180)}{\sigma(90)}$
$\frac{1}{2}(1+Px)$	1.18	Y	0	9.0	0	.77	0	.39	3.25	3.25	23.1	.15	1.26
$\frac{1}{2}(1+Px)$	1.18	Y	5.6	9.9	0	.75	0	.04	2.91	2.91	-	-	-
$\frac{1}{2}(1+Px)$	1.35	Y	0	9.3	0	.98	0	.57	4.6	4.6	22.9	.21	1.45
$\frac{1}{2}(1+Px)$	1.35	Y	1.9	10.2	0	.78	0	.14	3.20	3.20	23.1	.24	1.46
$(.37+.63Px)S_{12}$*	1.35	Y	1.9	10.7	-.20	.70	.12	.12	3.04	2.95	-	-	-
$(.24+.76Px)S_{12}$*	1.35	Y	1.9	12.0	-.35	.66	.24	.06	2.61	2.46	-	-	-
.45 + .55Px	1.35	Y	1.9	10.3	-.16	.78	-.02	.15	3.52	2.84	-	-	-
.4 + .6Px	1.35	Y	1.9	10.4	-.32	.77	-.05	.16	3.78	2.48	-	-	-
$\frac{1}{2}(1+Px)$	0.7	E	0	7.9	0	.99	0	.39	4.00	4.00	21.5	.17	1.30
.45 + .55Px	0.7	E	0	7.9	-.10	.99	-.07	.39	4.33	3.69	-	-	-
.4 + .6Px	0.7	E	0	8.0	-.20	1.00	-.16	.41	4.68	3.39	-	-	-
$\frac{1}{2}(1+Px)$	0.75	E	1.8	8.7	0	.92	0	.03	3.8	3.8	21.7	.18	1.33
$-\frac{1}{3}(\sigma_1\sigma_2)(\tau_1\tau_2)$	2.0	S	0	7.1	-.86	1.13	-.34	.12	9.57	1.59	21.3	.11	1.42
$-\frac{1}{3}(\sigma_1\sigma_2)(\tau_1\cdot\tau_2)$	1.8	S	0	7.4	-.61	.63	-.19	.05	3.50	1.30	22.2	.04	1.14
EXPERIMENTAL VALUE				7.9±1.0	-.14±.10	.73±.10	.08±.10	.17±.10	3.6±.6	3.0±1.0	19.4±2.0	.26±.10	1.55±.20

*The exchange dependence for the central force is $\frac{1}{2}(1+Px)$.

Table 3. High energy scattering behavior of various models. In the above the range (R) is the same in singlet and triplet states. For all cases where $\gamma \neq 0$, γ is adjusted to $Q = 2.73 \times 10^{-27}$ cm^2. σ is the total cross section, the differential cross section being $4\pi\sigma(\theta) = \sigma \cdot \sum a_n P_n(\theta)$, where $a_0 = 1$.

Table 4

Properties of Selected Yukawa Potentials

Central range (10^{-13} cm)	Tensor range (10^{-13} cm)	γ	W_D	${}^3\rho$ (10^{-13} cm)	${}^3r$ (10^{-13} cm)	${}^3T$ (10^{-39} cm^3)	${}^3a$ (10^{-13} cm)
1.18	1.18	5.6	5.3	1.56	1.48	.3	5.22
1.18	1.69	0.8	3.2	1.71	1.49	1.0	5.29
1.18	1.98	0.5	2.8	1.76	1.50	1.2	5.30
1.18	3.91	0.16	1.7	1.90	1.45	2.1	5.35
1.18	(No tensor force)	--	--	1.67	1.54	.6	5.29
1.35	1.35	1.91	4.2	1.71	1.58	.55	5.32
1.35	(No tensor force)	--	--	1.85	1.63	.96	5.39

In the above ${}^3\rho$ is the effective range as determined by using the deuteron wave function. ${}^3T$, the shape dependent coefficient, has been determined from the approximate relation ${}^3T = \frac{1}{4}({}^3r)^2({}^3\rho - {}^3r)$, and checked by neglecting in the exact expression for ${}^3T$ all terms involving the coupled D state(24). All the above potentials gave a value of 0.28 (within 2 percent) for the ratio of the cross sections for photomagnetic to photoelectric disintegrations of the deuteron for the 2.76 Mev Na γ ray using a value of 2.23 Mev as the binding energy of the deuteron. (For experimental values see Ref. 25).

Table 5

Comparison of Contributions of Various States to Total Cross Section

State	Square well		Yukawa	
	Tensor forces (10^{-26} cm^2)	Central forces (10^{-26} cm^2)	Tensor forces (10^{-26} cm^2)	Central forces (10^{-26} cm^2)
$^3S_1$	2.95^+	3.25^+	8.82^+	9.58^+
$^3D_1$	0.35^-	0.95^+	0.55^-	0.14^+
$^3D_2$	5.87^+	1.58^+	1.82^+	0.24^+
$^3D_3$	0.72^+	2.21^+	0.14^-	0.33^+

References

1. L. Rosenfeld, Nuclear Forces, Vol. 2, Interscience Pub., New York, page 311 et seq. It might appear at first sight that corrections due to spin orbit coupling are of order v/c. Actually in a field theory calculation corrections which introduce this coupling include also a gradient of the potential (e.g., the Thomas term for the hydrogen atom) which in scattering produces an additional factor of v/c.

2. H. Snyder and R. E. Marshak, Phys. Rev. 72, 1253 (1947).

3. R. G. Sachs, Phys. Rev. 72, 91 (1947)
H. Primakoff, Phys. Rev. 72, 118 (1947)
G. Breit and I. Bloch, Phys. Rev. 72, 135 (1947)

4. R. B. Sutton et al., Phys. Rev. 72, 1147 (1947)

5. C. G. Schull et al., Phys. Rev. 73, 842 (1948)

6. W. B. Jones, Jr., Phys. Rev. 74, 364 (1948)
E. Melkonian, L. J. Rainwater, W. W. Havens, Jr., Bull. Am. Phys. Soc. 24, No. 1, Paper G1 (1949)

7. R. E. Bell and L. G. Elliot, Phys. Rev. 74, 1552 (1948)
W. E. Stephens, Rev. Mod. Phys. 19, 19 (1947)
W. E. Stephens, Bull. Am. Phys. Soc. 24, No. 4, Paper T1 (1949)
A. N. Tollestrup, et al., Phys. Rev. 75, 1947 (1949)

8. A. Nordsieck, Phys. Rev. 58, 310 (1940)

9. J. Hadley, et al., Phys. Rev. 75, 351 (1949)

10. R. H. Hildebrand and C. E. Leith, Bull. Am. Phys. Soc. 24, No. 6, Paper C8 (1949); also private communication.

11. L. J. Cook, et al., Phys. Rev. 72, 1264 (1947)

12. J. DeJuren, N. Knable, and B. Moyer, Bull. Am. Phys. Soc. 24, No. 6, Paper E9 (1949)

13. K. Brueckner, et al., Phys. Rev. 75, 555 (1949)

14. R. E. Langer, Phys. Rev. 51, 669 (1937)

15. N. Svartholm, "The Binding Energies of the Lightest Atomic Nuclei," Lund (1945)
J. Schwinger, Phys. Rev. 72, 742 A (1947), and hectographed Notes on Nuclear Theory, Harvard (1947)

References (Continued)

16. J. M. Blatt, Phys. Rev. 74, 92 (1948)
J. M. Blatt and J. D. Jackson, Phys. Rev. 76, 18 (1949)

17. C. D. Bailey, et al., Phys. Rev. 70, 583 (1946)

18. Professor J. H. Williams has kindly communicated to us more recent values of the experiments of E. E. Lampi, G. Freier and J. H. Williams, Bull. Am. Phys. Soc. 24, No. 4, Paper X6 (1949). Further experiments are still in progress.

19. W. Sleator, Jr., Phys. Rev. 72, 207 (1947)

20. R. Sherr, Phys. Rev. 68, 240 (1945)

21. The results for $R = 1.185 \times 10^{-13}$ cm are in agreement with those from more precise calculations communicated to the authors by H. Feshbach.

22. W. Rarita and J. Schwinger, Phys. Rev. 59, 436 (1941)

23. W. Hefner and R. Peierls, Proc. Roy. Soc. 181, 43 (1942)

24. R. Christian, Phys. Rev. 75, 1675 (1949)

25. W. M. Woodward and I. Halpern, Phys. Rev. 76, 107 (1949)
E. Meiners, Phys. Rev. 76, 259 (1949)

26. E. Kelly, C. Leith and C. Wiegand, Bull. Am. Phys. Soc. 24, No. 6, Paper E8 (1949)

27. H. H. Barschall and R. F. Taschek, Phys. Rev. 75, 1819 (1949)

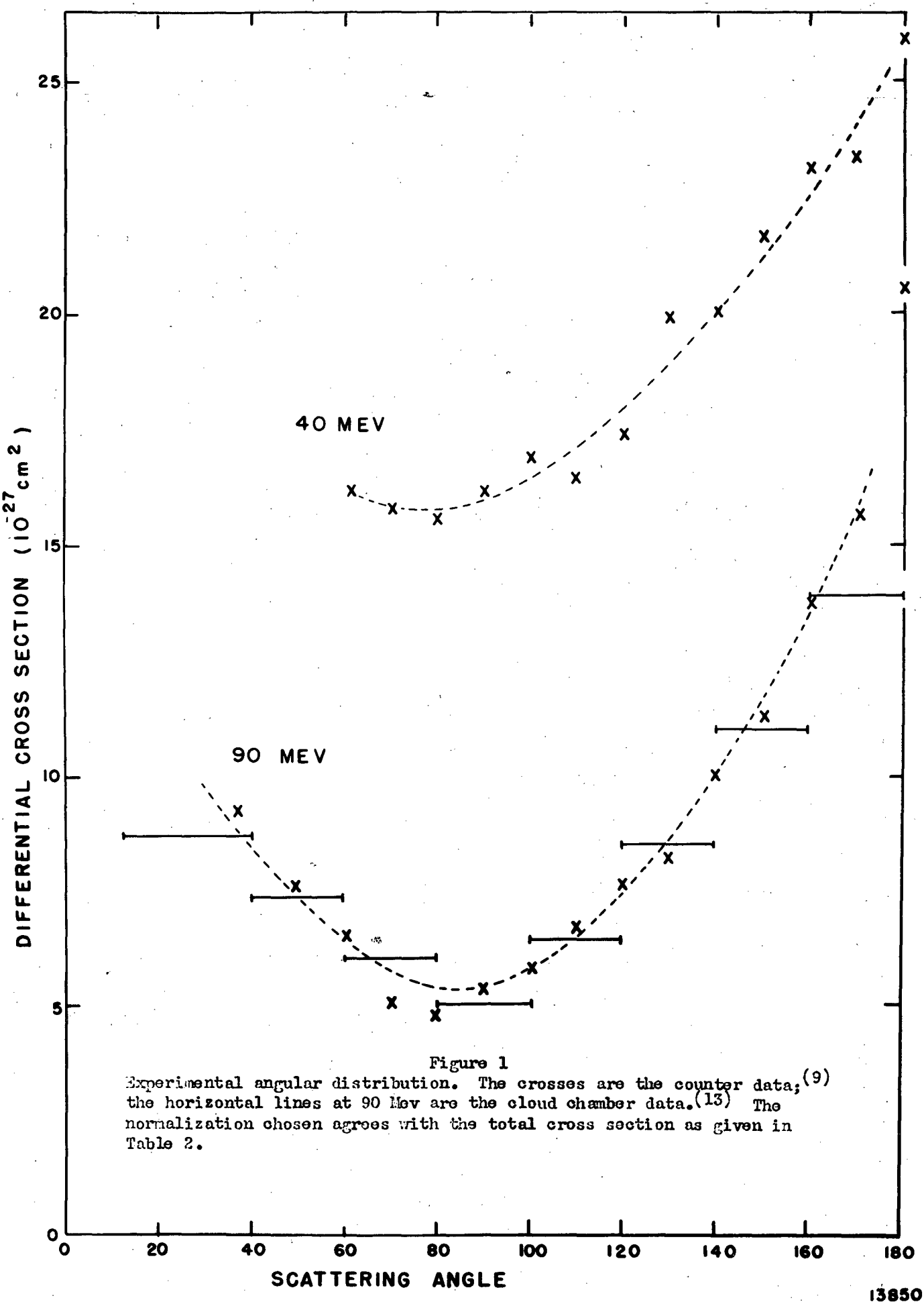

Figure 1
Experimental angular distribution. The crosses are the counter data;[9] the horizontal lines at 90 Mev are the cloud chamber data.[13] The normalization chosen agrees with the total cross section as given in Table 2.

13850-1

02 660

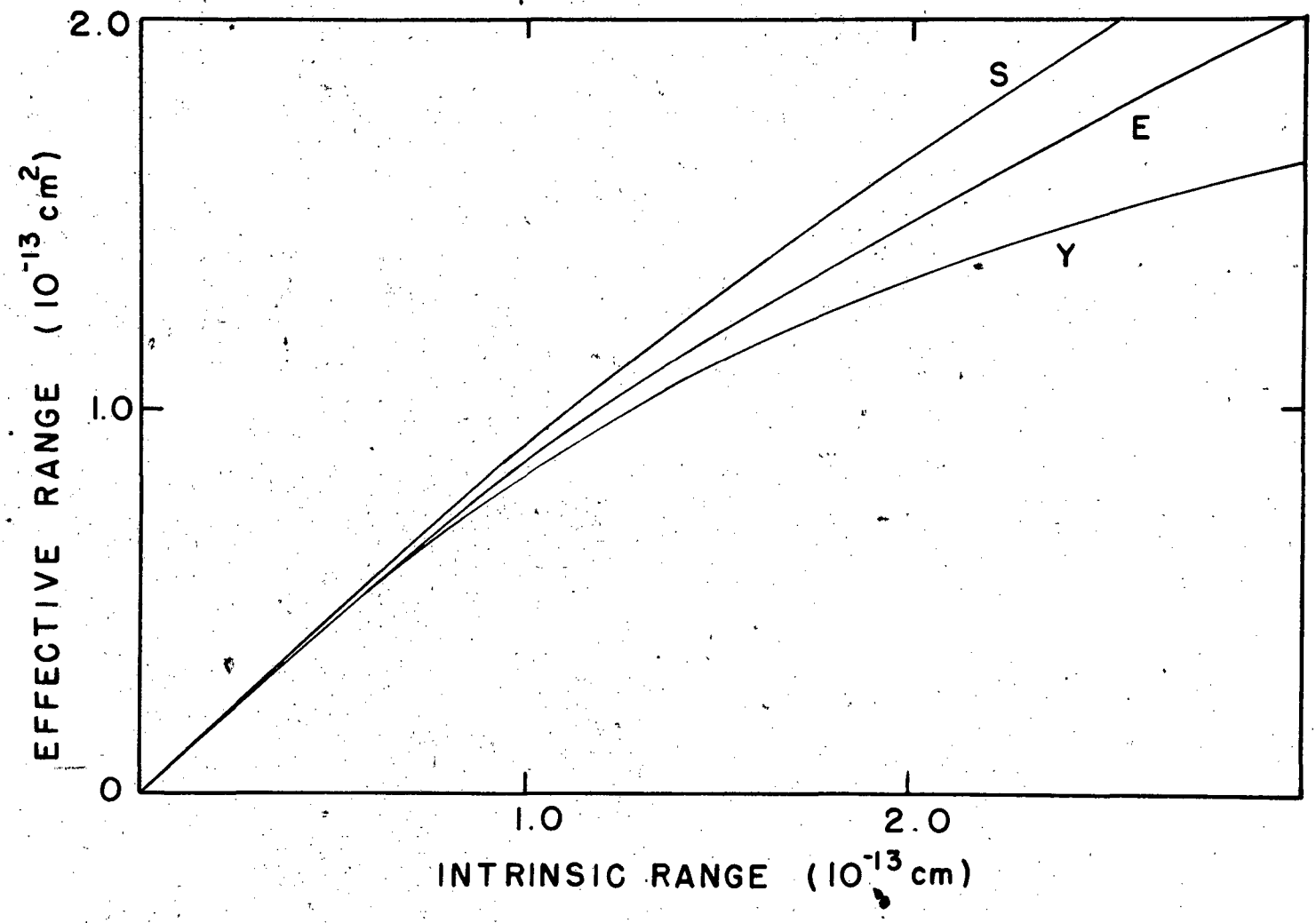

Figure 2

The triplet effective range for the Yukawa (Y), exponential (E), and the square well (S) potentials. The intrinsic range is 2.12 R, 3.54 R, and R for the three potentials in the order named above. R is the usual parametric range that occurs in the radial dependence, i.e., $R/r\ e^{-r/R}$, $e^{-r/R}$ for the Yukawa and exponential potentials and a constant potential extending a distance R for the square well potential.

FIG. 2

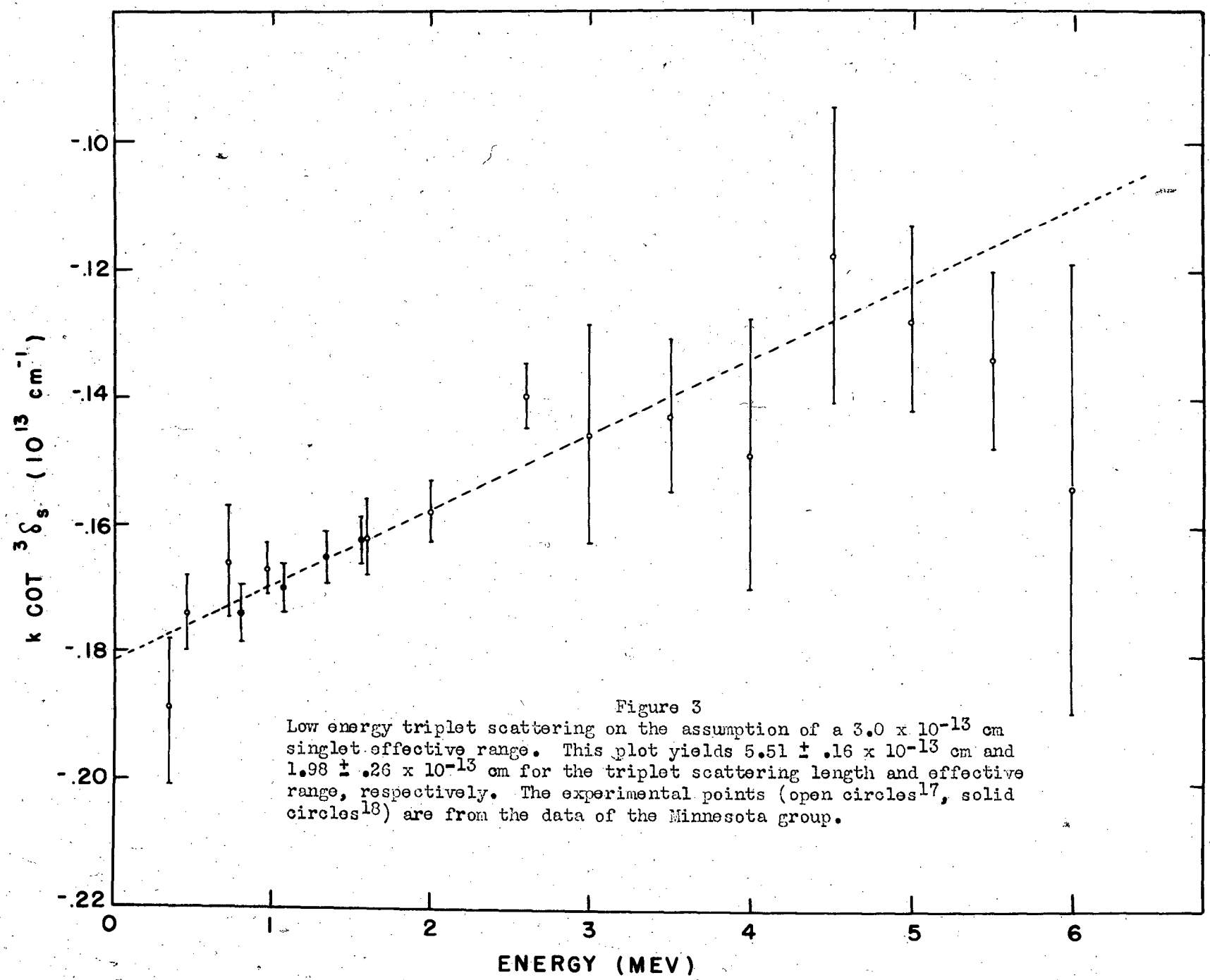

Figure 3
Low energy triplet scattering on the assumption of a 3.0 x 10^{-13} cm singlet effective range. This plot yields 5.51 ± .16 x 10^{-13} cm and 1.98 ± .26 x 10^{-13} cm for the triplet scattering length and effective range, respectively. The experimental points (open circles[17], solid circles[18]) are from the data of the Minnesota group.

FIG. 3

13851-1

02 672

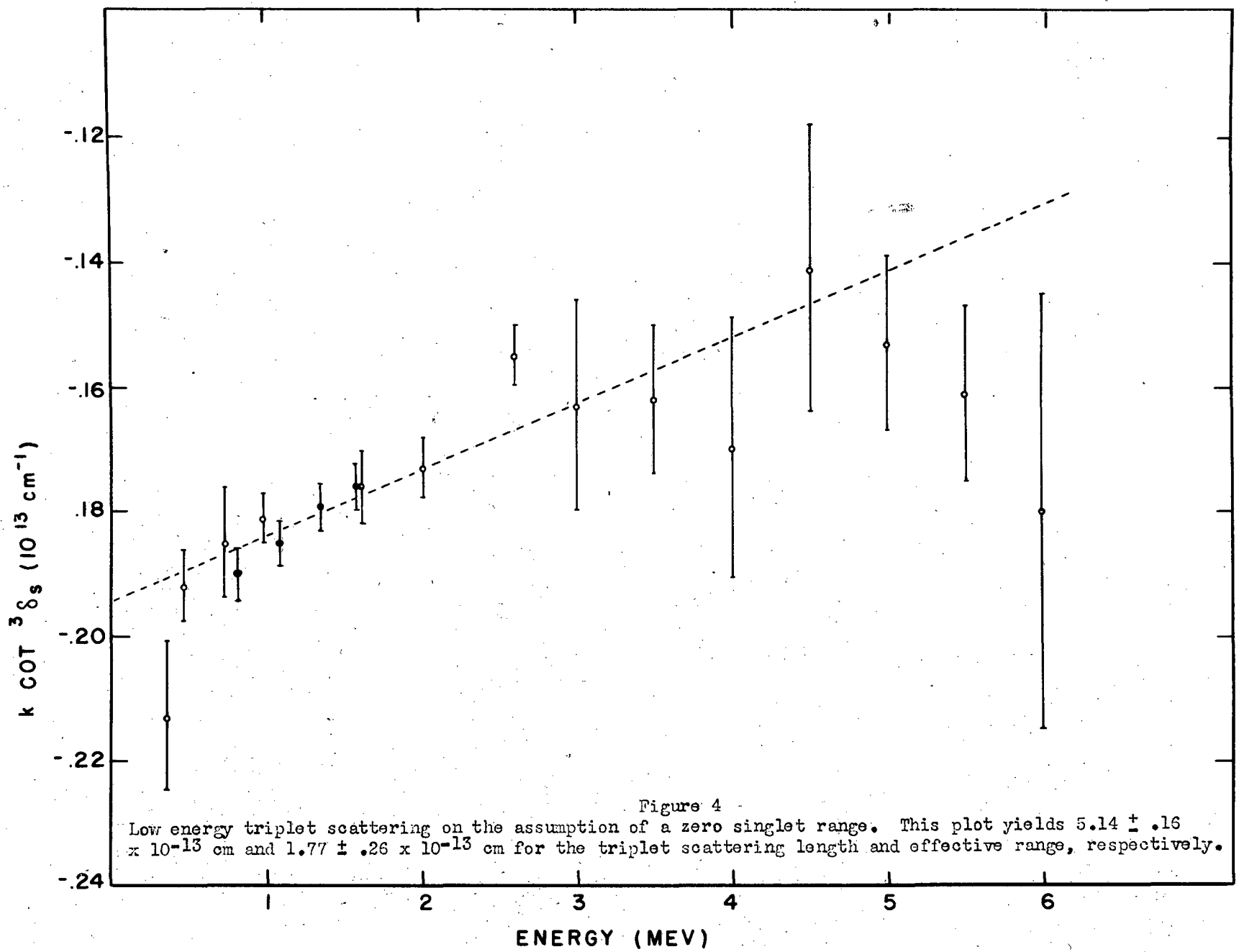

Figure 4
Low energy triplet scattering on the assumption of a zero singlet range. This plot yields 5.14 ± .16 x 10^{-13} cm and 1.77 ± .26 x 10^{-13} cm for the triplet scattering length and effective range, respectively.

FIG. 4

13852-1

02 668

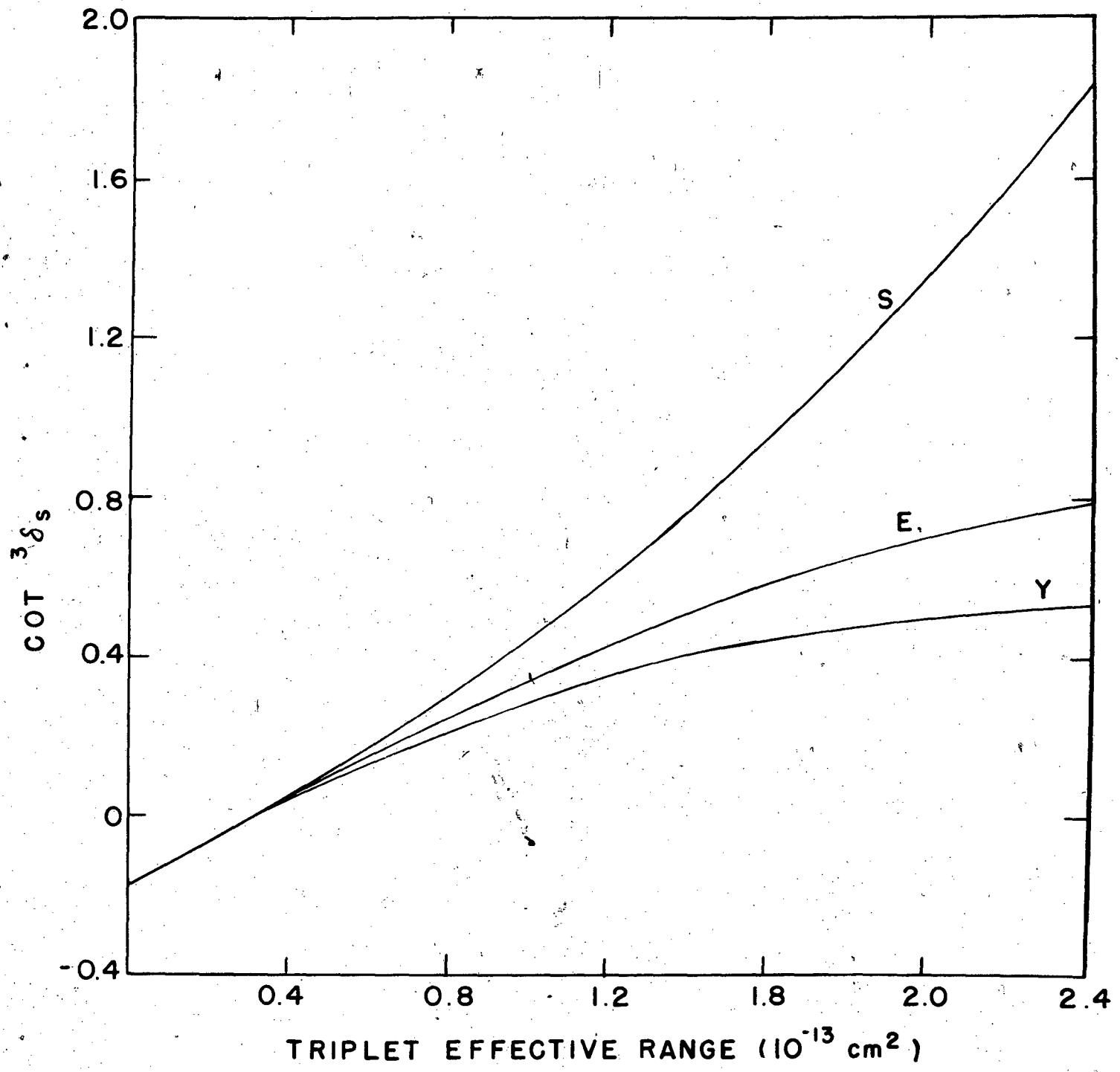

Figure 5
Triplet S-wave scattering at 90 Mev.

FIG. 5

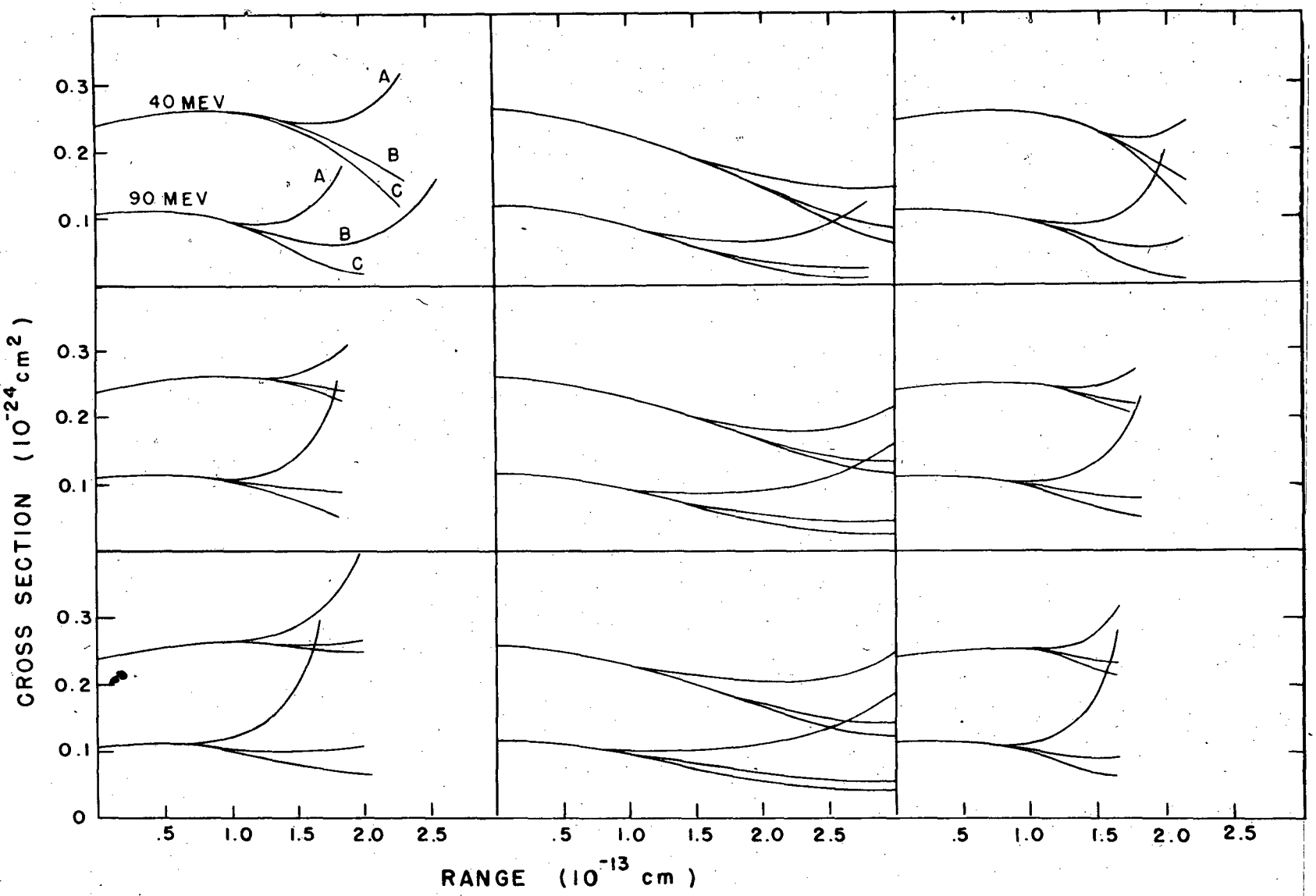

Figure 6

Central force scattering at 40 and 90 Mev. The first column gives the triplet scattering; the second, the singlet scattering; and the third, the complete scattering (assuming equal intrinsic ranges). The first row is for the square well; the second, for the exponential; and the third, for the Yukawa potential. In each figure the upper set of 3 curves is for 40 Mev; the lower, for 90 Mev. For each set of 3 curves the uppermost is $4\pi \cdot \sigma(180^\circ)$; the middle curve is the total cross section; and the lower is $4\pi \cdot \sigma(90^\circ)$. (Illustrated in the first figure by A, B, and C, respectively.) In all cases the exchange dependence is assumed to be $\frac{1}{2}(1 + P_x)$ (therefore, $\sigma(180^\circ) = \sigma(0^\circ)$), and the depths are chosen to fit the deuteron and the zero energy scattering.

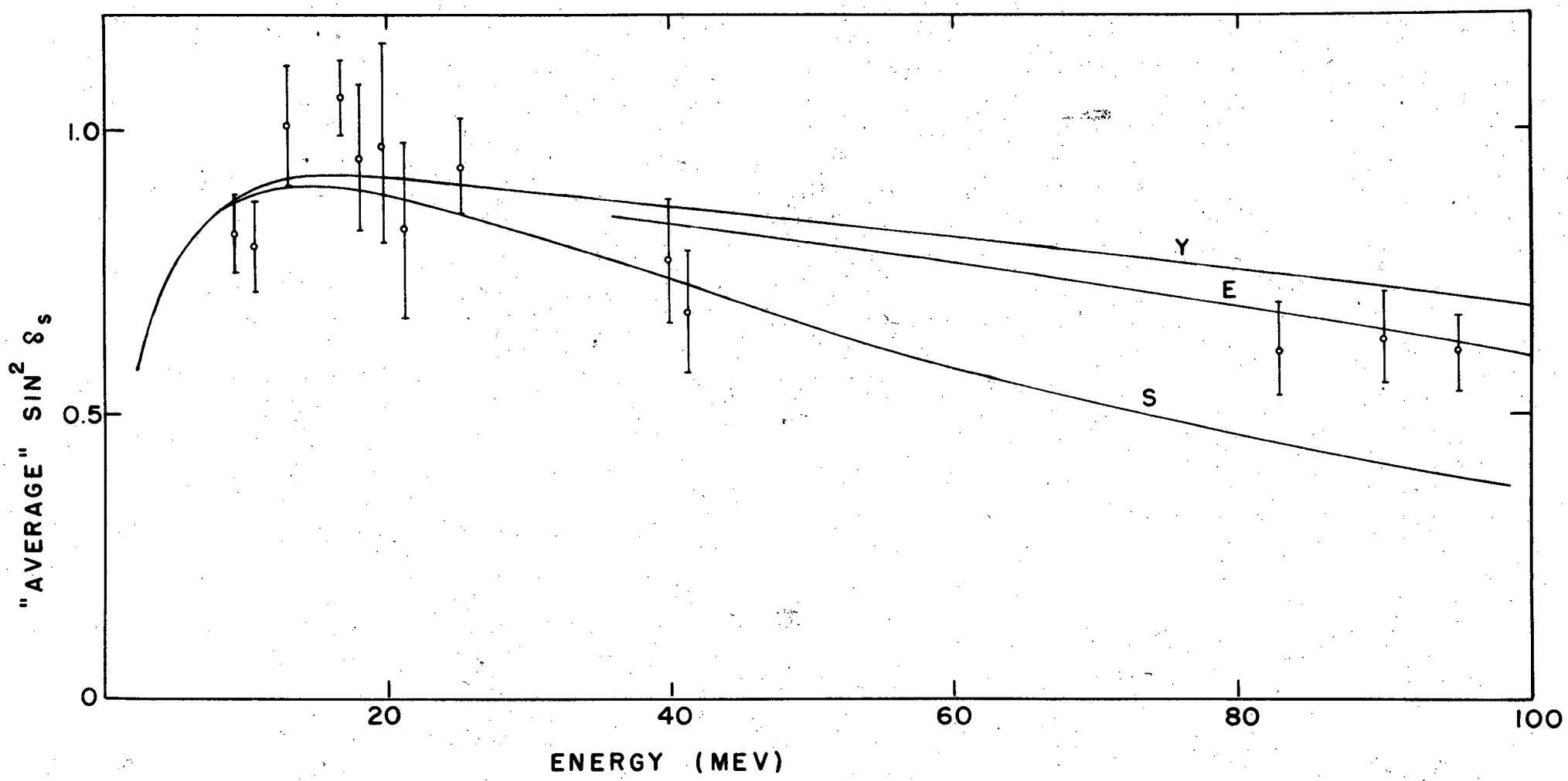

Figure 7

S-wave scattering phase shift, illustrated for a triplet effective range of 1.65×10^{-13} cm and a singlet effective range of 3.0×10^{-13} cm. Y, E, and S refer to the Yukawa, exponential and square well central potentials, respectively. The experimental points below 25 Mev are from the data of Sleator[18] and Sherr[19] (above 40 Mev, cf. Table 2).

FIG. 7

13855

02 674

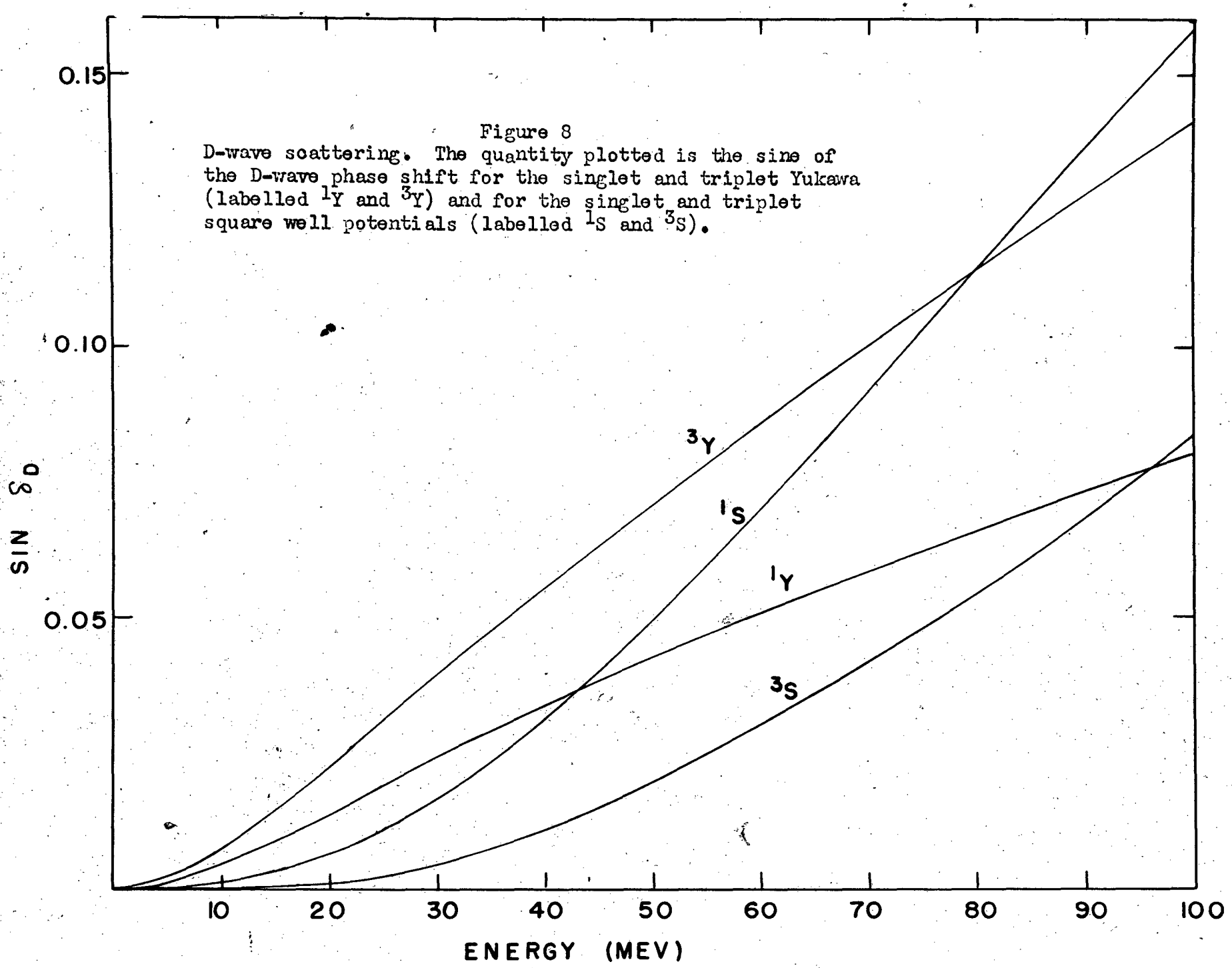

Figure 8
D-wave scattering. The quantity plotted is the sine of the D-wave phase shift for the singlet and triplet Yukawa (labelled ^1Y and ^3Y) and for the singlet and triplet square well potentials (labelled ^1S and ^3S).

FIG. 8

02 662

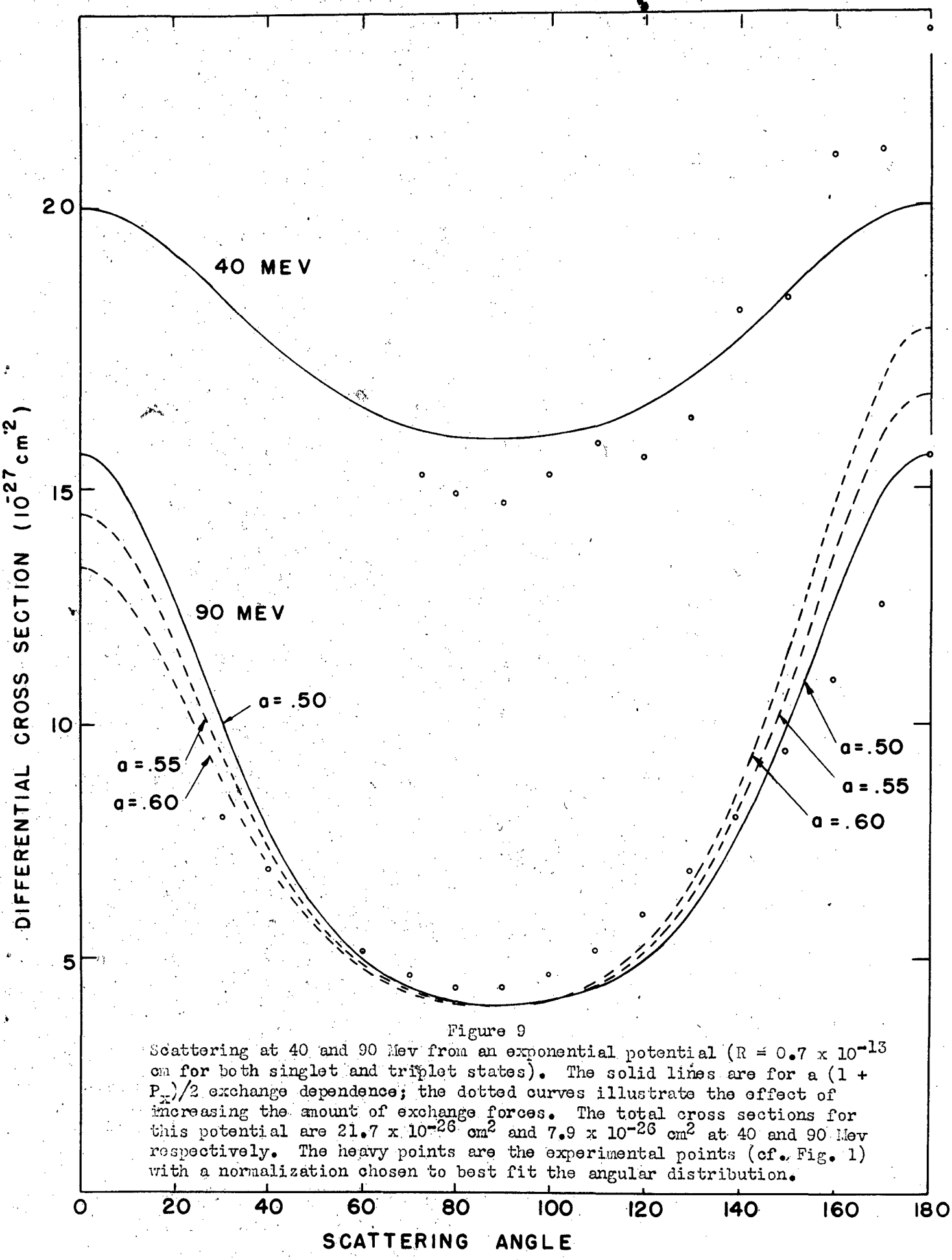

Figure 9

Scattering at 40 and 90 Mev from an exponential potential ($R = 0.7 \times 10^{-13}$ cm for both singlet and triplet states). The solid lines are for a $(1 + P_x)/2$ exchange dependence; the dotted curves illustrate the effect of increasing the amount of exchange forces. The total cross sections for this potential are 21.7×10^{-26} cm^2 and 7.9×10^{-26} cm^2 at 40 and 90 Mev respectively. The heavy points are the experimental points (cf. Fig. 1) with a normalization chosen to best fit the angular distribution.

FIG. 9

13857 - I

02 666

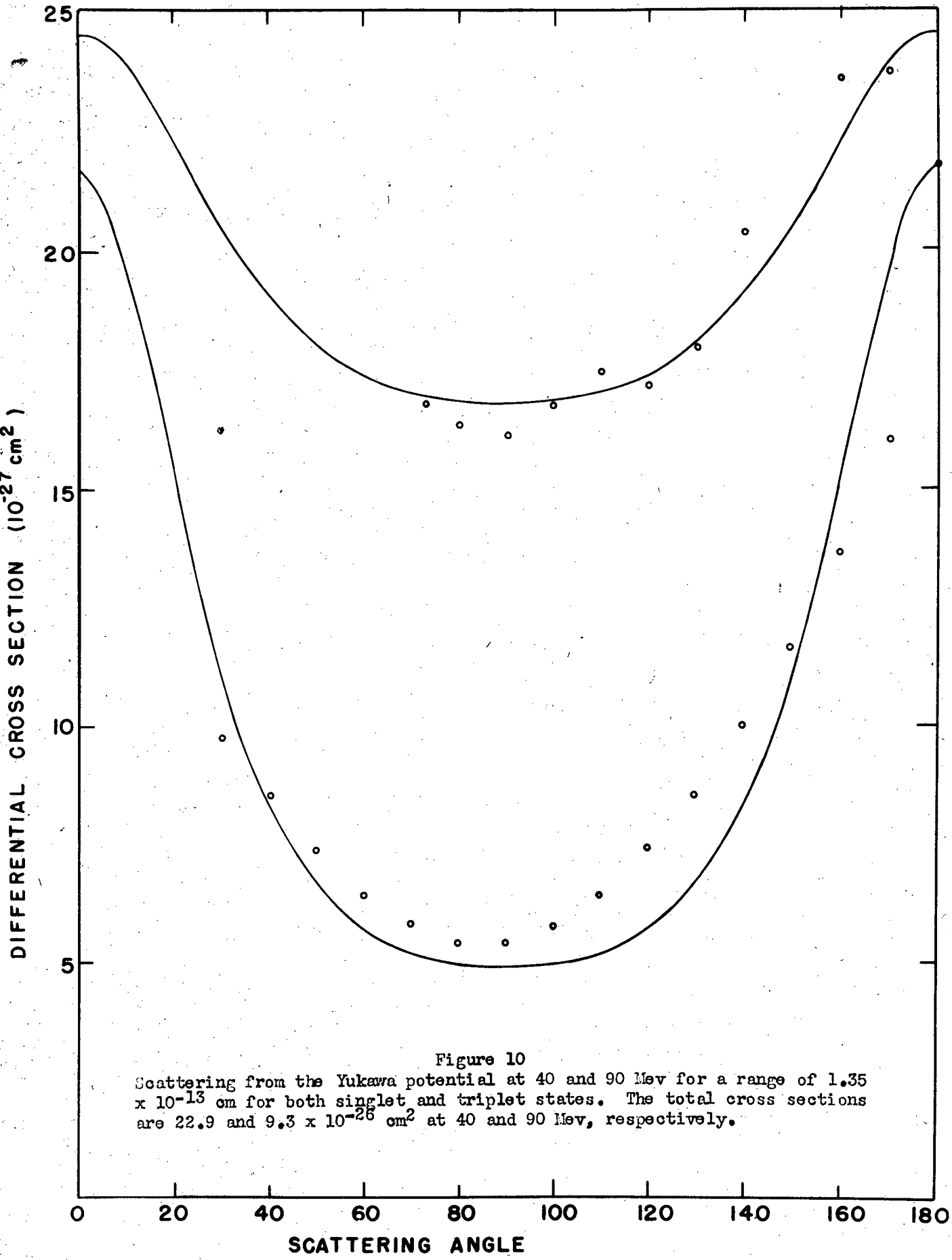

Figure 10
Scattering from the Yukawa potential at 40 and 90 Mev for a range of 1.35 x 10^{-13} cm for both singlet and triplet states. The total cross sections are 22.9 and 9.3 x 10^{-26} cm^2 at 40 and 90 Mev, respectively.

FIG. 10

13858 -1

02 675

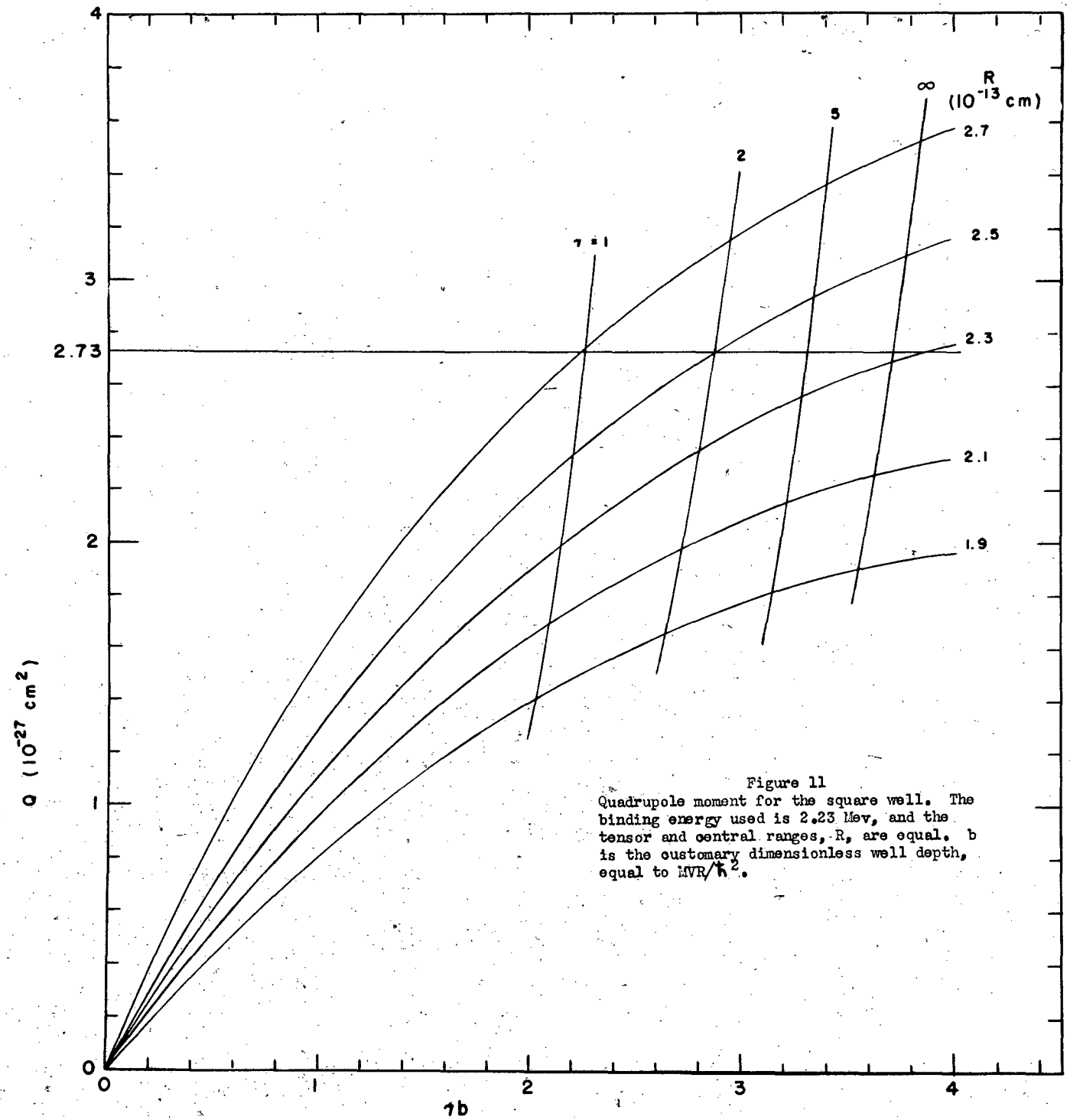

Figure 11
Quadrupole moment for the square well. The binding energy used is 2.23 Mev, and the tensor and central ranges, R, are equal. b is the customary dimensionless well depth, equal to $MVR/\hbar^2$.

FIG. 11

KODAK SAFETY I

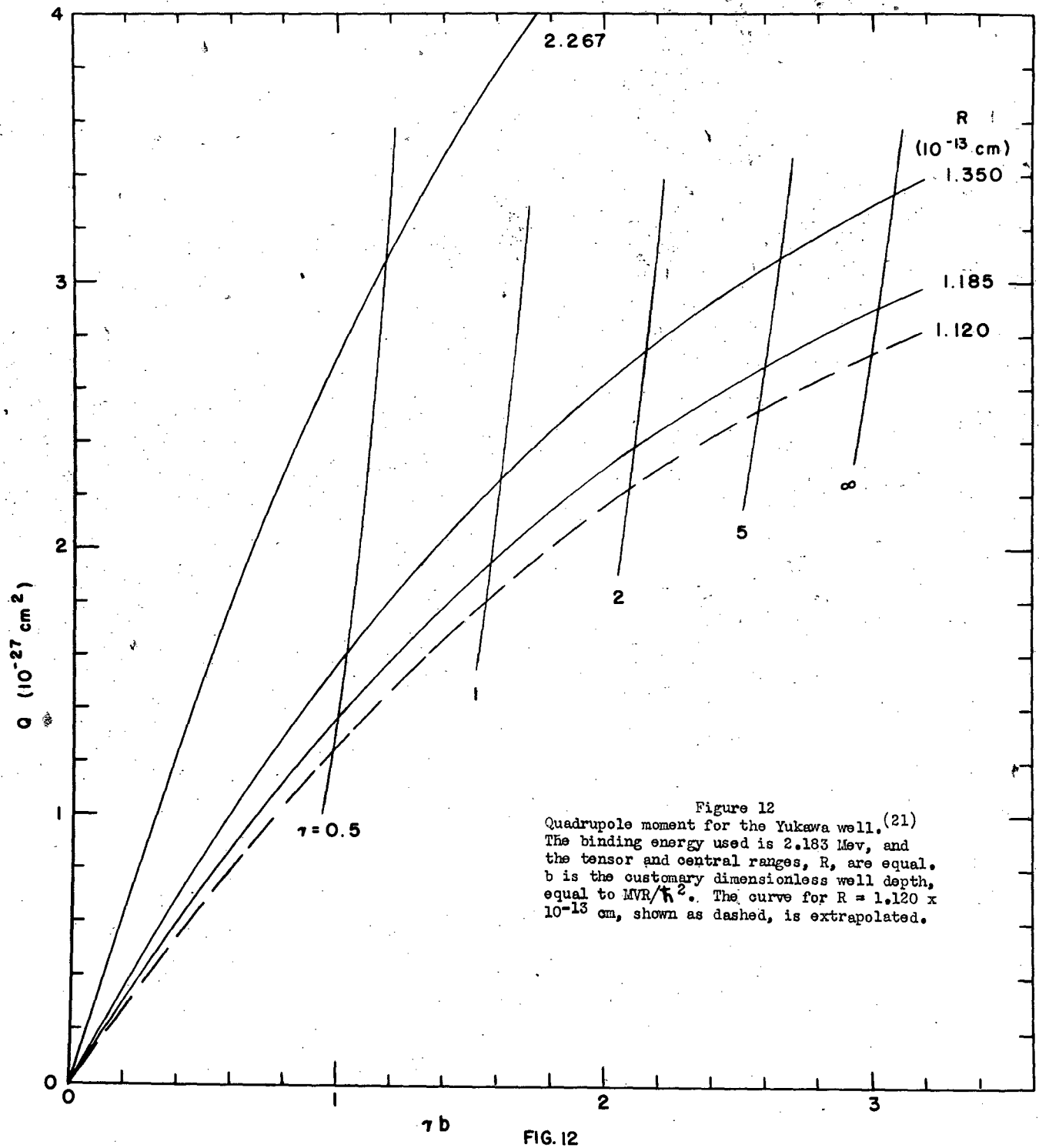

Figure 12
Quadrupole moment for the Yukawa well.[21] The binding energy used is 2.183 Mev, and the tensor and central ranges, R, are equal. b is the customary dimensionless well depth, equal to $MVR/\hbar^2$. The curve for R = 1.120 x 10^{-13} cm, shown as dashed, is extrapolated.

FIG. 12

02 673

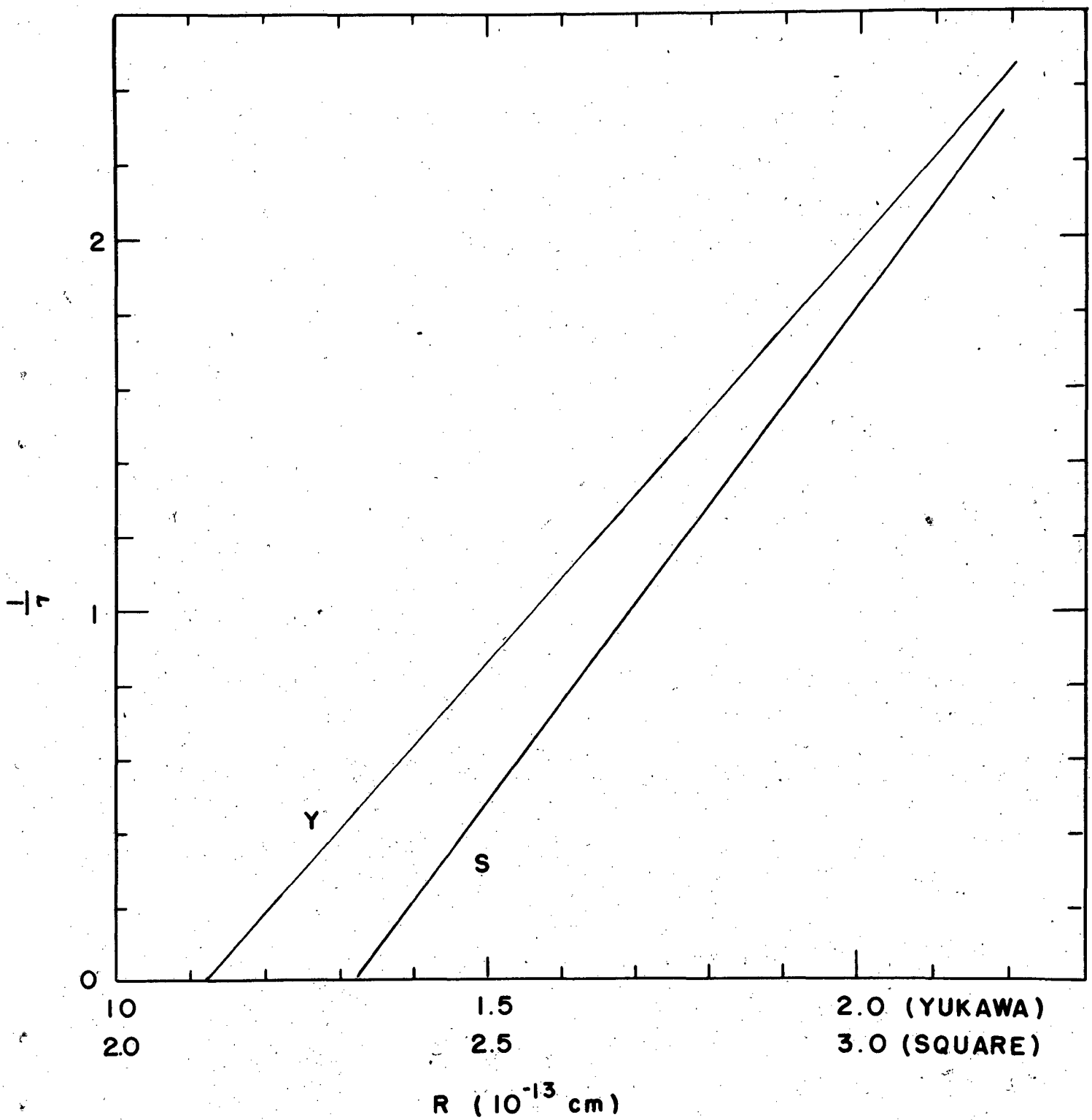

Figure 13
Ratio of central well depth to tensor well depth for quadrupole moment equal to 2.73×10^{-27} cm^2. The binding energy fitted for the Yukawa (Y) case is 2.183 Mev and for the square well (S) case is 2.23 Mev.

FIG. 13

13861-1
02 661

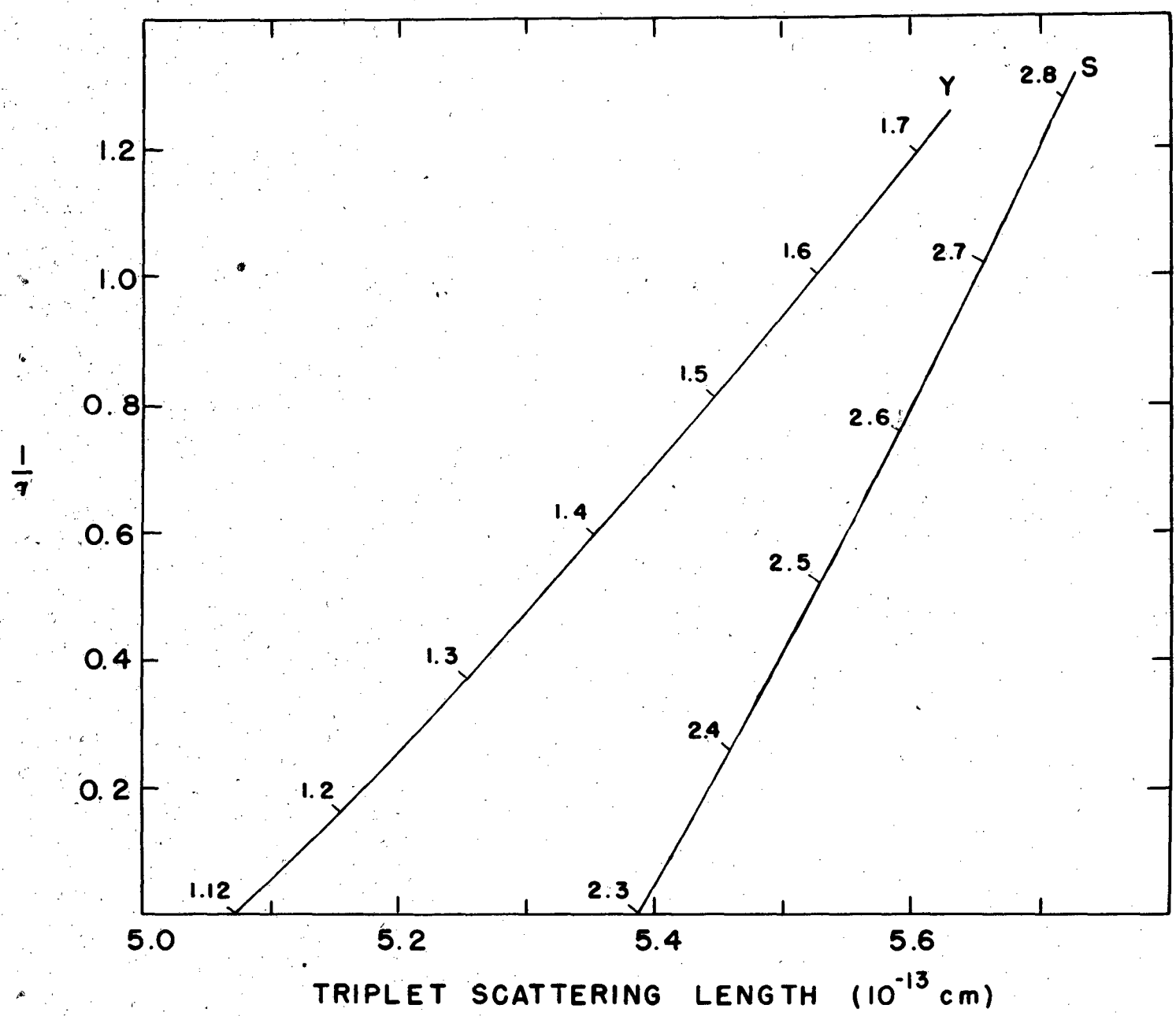

Figure 14
Low energy scattering with tensor forces for the Yukawa (Y) and the square well (S) potentials. The range is indicated (in units of 10^{-13} cm) parametrically along the curves. (Depths are adjusted to fit the binding energy and the quadrupole moment of the deuteron).

FIG. 14

02 664

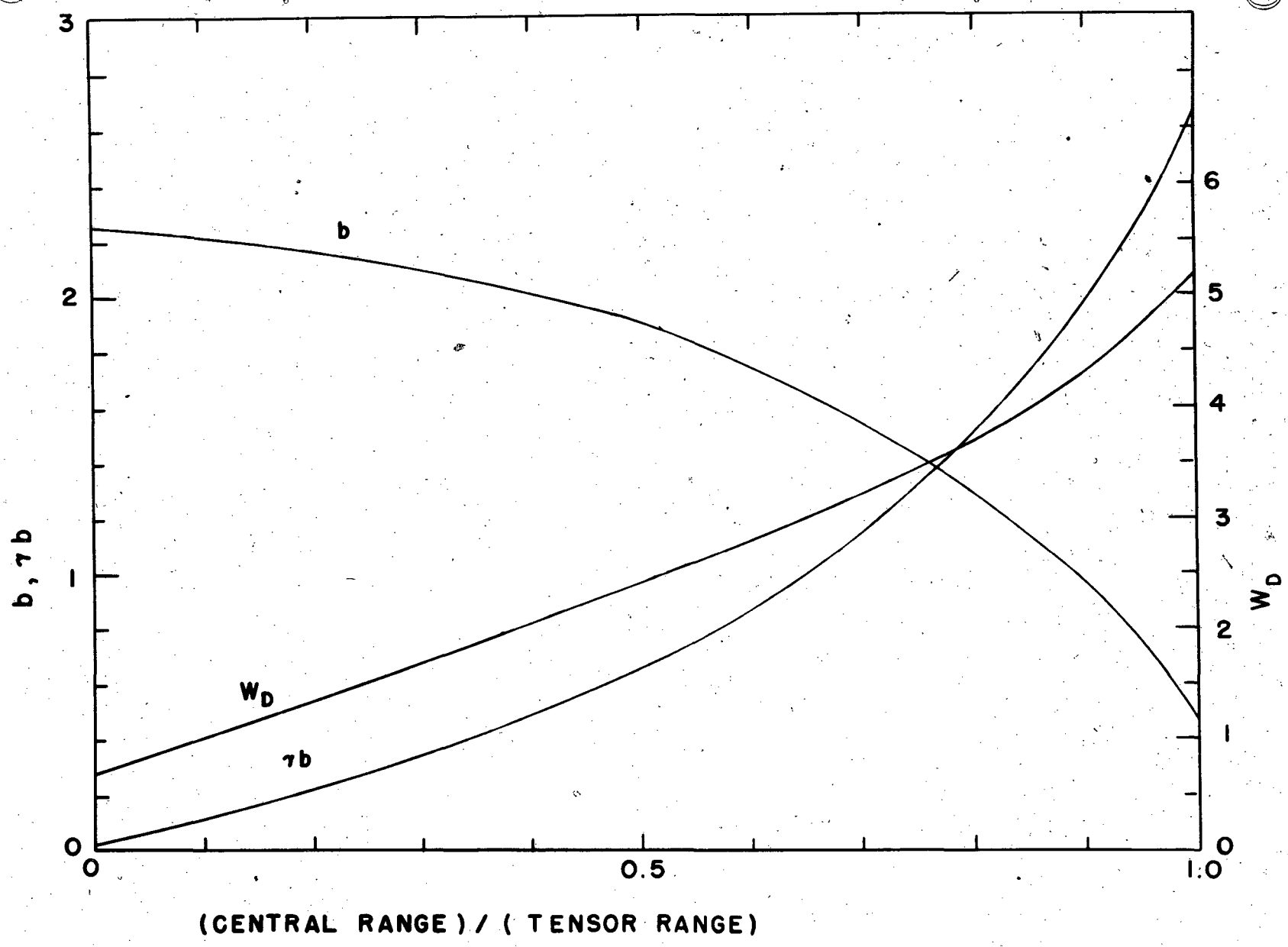

Figure 15

Variation of deuteron fitting parameters for increase of tensor range. The interaction is that of the Yukawa well for which the central range is 1.185×10^{-13} cm. W_D is the percentage of D state; b is the dimensionless central well depth equal to $MVR^2/\hbar^2$; γb is the tensor well depth. The binding energy fitted is 2.183 Mev.

02 677

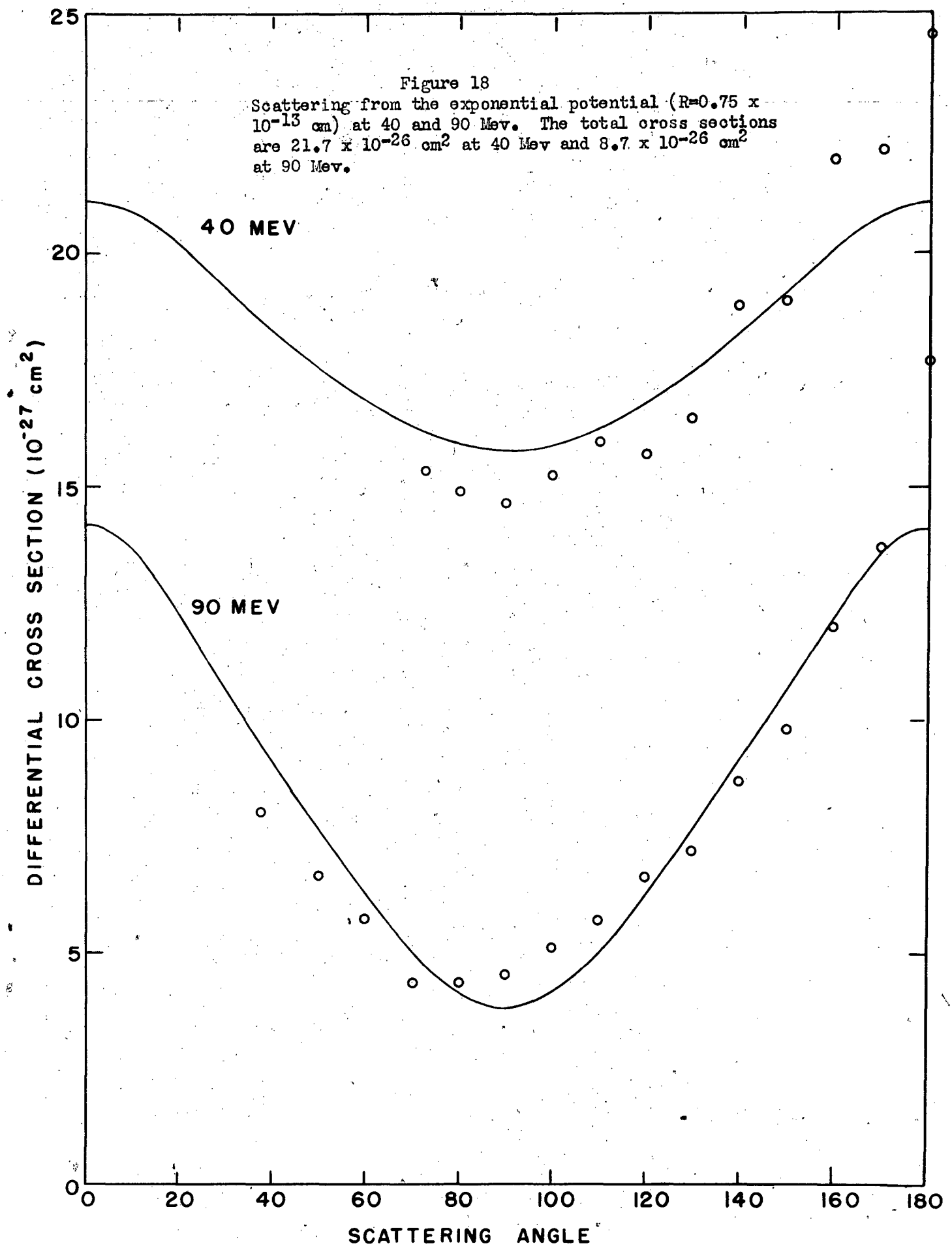

Figure 18
Scattering from the exponential potential ($R=0.75 \times 10^{-13}$ cm) at 40 and 90 Mev. The total cross sections are 21.7×10^{-26} cm^2 at 40 Mev and 8.7×10^{-26} cm^2 at 90 Mev.

FIG.18

13999-1

02 667

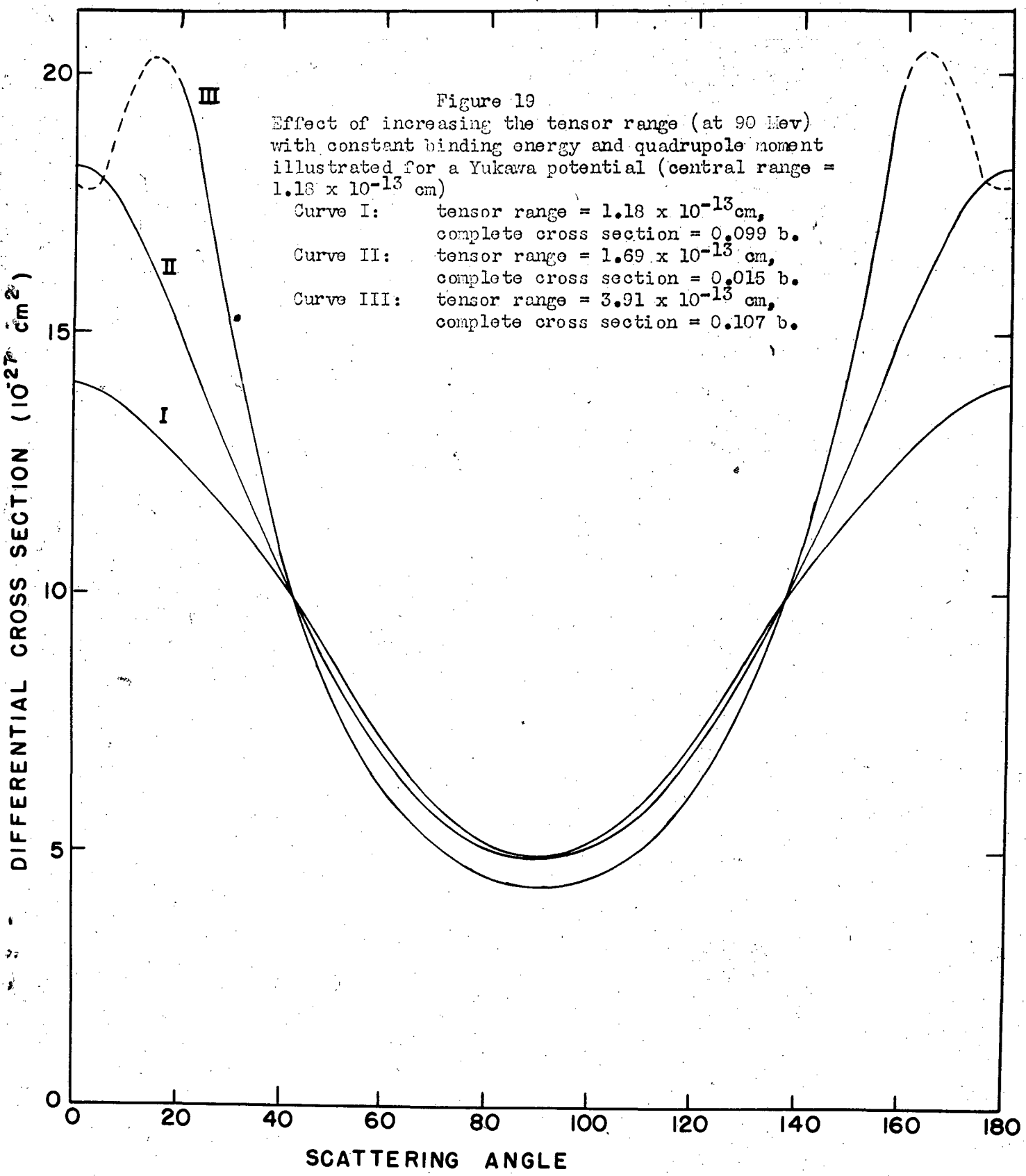

FIG. 19

13866-1

02 671